UPDATE: STRUCTURAL UNCERTAINTY OF USED NUCLEAR FUEL IN DRY STORAGE CANISTERS

Fuel Cycle Research & Development

Prepared for
U.S. Department of Energy
Used Fuel Disposition Campaign

Nicholas A Klymyshyn
Nathan P Barrett
Kenneth I Johnson
Brady D Hanson
Pacific Northwest National Laboratory
September 11, 2015

FCRD-UFD-2015-000493
PNNL-24669

Reviewed by:

Project Manager

Brady Hanson (signature on file)
Name

SUMMARY

This report fulfills the M3 milestone M3FT-15PN0810047 “Structural Uncertainty Update” under work package FT-15PN081004.

The Structural Uncertainty research task uses numerical modeling to help close knowledge gaps associated with extended dry storage of used nuclear fuel. Modeling helps to predict the expected range of mechanical loading on used nuclear fuel and dry storage system components, which is needed to help guide materials research. Knowledge of expected loads helps the materials researchers prioritize their research and focus only on the relevant material degradation phenomena that can have an effect on the ability of dry storage systems to function. The loads considered in this task are dry storage cask (DSC) tip-over, handling drops of the multipurpose fuel canister, and seismic loading of DSC systems while situated on the concrete pad of a storage facility.

This document is a progress report that describes the work that was performed in fiscal year 2015. The work is a broad task that considers a number of physical phenomena and uses sophisticated LS-DYNA finite element models to predict used fuel and DSC system response to dynamic loads. Due to the broad list of topics and limited budgets, the topics of this task are prioritized at the beginning of the year and the priorities are subject to revision throughout the year as the Pacific Northwest National Laboratory team collaborates with other members of the Used Fuel Disposition Campaign.

This year, three topics were investigated: options for modeling cladding in LS-DYNA, the effect of cladding thinning in the tip-over load case, and stress corrosion cracking in multipurpose canister welds. In each of these cases, significant progress was made. This report details the work that was done and identifies areas where more work is needed.

The cladding modeling options study investigated a number of features that are available to model fuel cladding as beam elements in LS-DYNA. Beam element formulations and material property capabilities, such as strain rate dependent plasticity capabilities, were explored. An evaluation of beam element accuracy was performed against closed form solutions and showed that the default beam formulation has error bands of ±5%, while the best and most computationally expensive options can achieve an error band within ±1%.

The cladding thinning task is concerned with identifying the amount of cladding thinning that is permissible in the three characteristic load cases of this study: tip-over, handling drop, and seismic response. The tip-over case was the first load case that was chosen because it calculated the highest loads on the cladding in the previous year. The previous year’s model was upgraded based on the results of the cladding modeling options study so it used the most accurate beam element formulation. However, making this change resulted in an unexpectedly large increase in peak cladding stress throughout the fuel assembly. It is too early to draw any conclusions for this case because additional review of the models is needed. The preliminary results are documented in this report. The intent is to resolve the modeling issues early next fiscal year and report final results next year. If time and budget are available, the cladding thinning study will also be extended to the handling drop and seismic load cases.

The topic of stress corrosion cracking was evaluated using the existing LS-DYNA finite element models of a DSC system in the tip-over load case. Again, the tip-over case was chosen as the first load case to be evaluated because it predicted the highest localized stresses in the canister weld regions. Elastic-plastic fracture and section collapse analyses were performed, which determined that failure of the weld region is expected to be through plastic collapse of the remaining wall section rather than crack propagation. Some additional LS-DYNA modeling was done to check the response of the canister when flaws were introduced. The results demonstrate that the canister containment boundary is generally resilient to localized flaws. Additional work is needed to apply the methodology that was developed this year to the handling drop and seismic load cases.

CONTENTS

FIGURES

TABLES

ACRONYMS

ASME	American Society of Mechanical Engineers
DSC	dry storage cask
EPRI	Electric Power Research Institute
FY	fiscal year
MPC	multipurpose canister
NRC	U.S. Nuclear Regulatory Commission
PNNL	Pacific Northwest National Laboratory
SCC	stress corrosion cracking
UFDC	Used Fuel Disposition Campaign

UPDATE: STRUCTURAL UNCERTAINTY OF USED NUCLEAR FUEL IN DRY STORAGE CANISTERS

1.0 INTRODUCTION

Used nuclear fuel storage and transportation pose a number of technical challenges. One of the major challenges is uncertainty in material behavior over extended periods of time. Although some literature exists on the properties of used nuclear fuel after coming out of the reactor environment, significant uncertainty still exists in the performance of used nuclear fuel and its storage and transportation systems (canister and internals) during extended periods. The goal of the Structural Uncertainty research task is to determine the amount of material degradation that is permissible in dry storage cask (DSC) system components under extended dry storage scenarios. The value of this numerical modeling study is to provide guidance to materials researchers on what material degradation phenomena require study. The ultimate purpose of this task is to assist in filling a knowledge gap in the realm of extended dry storage of used nuclear fuel.

This report documents the progress the Pacific Northwest National Laboratory (PNNL) made during fiscal year 2015 (FY15) and identifies the work that remains to be completed in future years. This research task began with a study of the structural sensitivity of DSC systems to dry storage mechanical loading scenarios presented in Klymyshyn et al. (2013). The task continued in 2014 with a focus on fuel assembly response in Klymyshyn et al. (2014a). This year, three topics were explored:

Cladding Modeling Options: Cladding is represented by beam finite elements in the PNNL's detailed fuel assembly model. Certain element formulations and material behavior features are available, including strain-rate-dependent material properties and elastic-plastic material behavior. The available options were explored, and the accuracy of cladding beam models was explored comparing to closed form solutions. PNNL fuel cladding test data was used as the basis for this cladding modeling study. This study has identified the element formulation with the greatest accuracy, and this will be implemented in PNNL fuel assembly models going forward for Used Fuel Disposition Campaign (UFDC) analyses. This study is documented in detail in Section 2.0.

Cladding Thinning: Last year's work on modeling fuel assemblies under DSC loading conditions predicted that the cladding would survive a cask tip-over load scenario without rupturing the cladding. This year's work focused on determining how much cladding thinning would need to occur to lead to failures in the cladding. The tip-over load case was re-evaluated using an upgraded cladding model (based on the results of the cladding modeling options study) and it was found that the upgraded model predicted cladding failure in the tip-over case without any cladding thinning. The model results require more evaluation to resolve the differences between the 2014 model and the 2015 model, so the current results documented in this report should be considered preliminary. The goal in 2016 is to resolve the model differences to verify that the numerical model provides an accurate prediction of cladding stresses and conclude the cladding thinning study for the tip-over, seismic, and handling drop load scenarios. Section 3.0 documents

the results of the tip-over model with updated fuel cladding elements, but this effort represents work in progress and is not the final analysis of the tip-over load case.

Stress Corrosion Cracking of Multipurpose Canister: The potential for stress corrosion cracking (SCC) in multipurpose canister (MPC) welds was evaluated for the tip-over load case. A methodology for evaluating crack propagation potential using LS-DYNA impact model results was developed. Additional modeling that considered the existence of flaws in the weld material was also performed. The study concludes that even in the presence of cracking, plastic deformation of the ductile 304 stainless steel canister body is the expected failure mode rather than elastic-plastic fracture. This study is presented in detail in Section 4.0.

After each topic is discussed separately, Section 5.0 discusses the conclusions that can be drawn from the current year's work.

2.0 CLADDING MODELING OPTIONS

PNNL has been using a highly detailed fuel assembly model for a number of UFDC studies of the past few years, including modeling support of the Sandia National Laboratories shaker table testing (Klymyshyn et al. 2014b), an estimation of fuel response to shock and vibration during normal conditions of rail transportation (Adkins et al. 2012), and estimation of fuel response to dry storage loading scenarios (Klymyshyn et al. 2014a). Beam elements are used in the detailed assembly model to represent the cladding and the guide thimbles, as beam elements represent the most computationally cost-effective way to model them. The fuel cladding beam section properties are typically defined to include the mass and stiffness of the fuel within the cladding as a composite beam. It was discovered last fiscal year that the beam modeling options could potentially influence the results of the tip-over load case, but additional study was necessary. There were also additional modeling issues related to fuel cladding to consider, including how to model strain-rate sensitivity in cladding material properties and how to model the cladding when plastic strain is predicted. To address these issues, a small-scale study was performed to test cladding modeling options and compare the results to closed-form solutions. This task was given priority this fiscal year because it influences a number of modeling efforts that are currently ongoing in the UFDC.

This study investigated the element formulation and material property definitions that were available in LS-DYNA to model a short section of fuel cladding that was oriented horizontally and subjected to a bending load. One end of the beam was fixed and a vertical downward force was applied to the free end. The geometry and material properties were drawn from recent PNNL cladding tests (Shimskey et al. 2014) to develop an accurate finite element model of the fuel cladding. In this case, the fuel is not included so the beam model represents an empty cladding tube that matches the configuration of the cladding segments from the test data. The most accurate model parameters, in descending order of effect on results, were the following:

- Belytschko-Schwer integrated beam element formulation
- Elastic material model
- 4x4 Gauss quadrature
- Shear factor = 0.3

Additionally, there was very little difference in the results when comparing the single-precision and double-precision LS-DYNA solvers for this small-scale study. PNNL typically evaluates the influence of numerical precision on a case-by-case basis.

2.1 Model Parameters

Properties collected during material tests were used to create a material model in LS-DYNA. Some work was done to translate the actual material properties into a form that LS-DYNA could use. This translation is discussed in the Material Model section below.

Next, the material model was applied to multiple analyses, each testing the effect that various model parameters have on the accuracy of the results. The parameters that were studied included the following element formulations, quadrature rules, shear factors, and applied loads.

Material Model	Element Formulation	Quadrature Rule	Shear Factor	Precision	Shape
• Power Law Plasticity • Plastic-Kinematic	• Hughes-Liu • Belytschko-Schwer	• 2x2 Gauss • 3x3 Gauss • 3x3 Lobatto • 4x4 Gauss	• 0.3 • 0.8 • 1.3	• Single • Double	• Tubular • Solid

Using various combinations of these values resulted in a number of different analyses that were run and compared. Mesh density was refined before altering the above variables. This eliminated the effects of mesh discretization on analysis accuracy. The final mesh used in all cases included 12 elements used in the 6 inch modeled cladding segment, which accurately matched the expected beam deformation. Further increase in mesh density did not improve the analysis results. The results from these analyses were collected and compared and are presented here.

2.2 Material Model

The material properties collected by experiment are shown in Table 2-1.

Table 2-1: Collected material properties.

E	9.93×10^6 psi	Young's modulus
K	1.05×10^9	Material strength coefficient
m	.015	Strain rate exponent
n	.127716	Strain hardening exponent
σ_y	79.5×10^3 psi	Yield stress
G	3.655×10^6 psi	Shear modulus
ν	.36	Poisson's ratio
ε_y	8×10^{-3}	Yield strain
UTS	87.97×10^3 psi	Ultimate tensile stress
ε_0	0.006	Strain rate before yield
$\dot{\varepsilon}$	0.0001	Strain rate

The following power law relationship between stress and strain was used as a best-fit curve with the collected experimental data.

$$\sigma = K \cdot \varepsilon^n \left(\frac{\dot{\varepsilon}}{10^{-3}} \right)^m$$

This equation very closely matches the Rate Sensitive Power Law Plasticity material model in LS-DYNA. However, LS-DYNA does not allow the use of the Rate Sensitive Power Law Plasticity with either Hughes-Liu or Belytschko-Schwer element formulations. Therefore, Hughes-Liu elements were used with the Power Law Plasticity material model. This model was used for two reasons. First, it is compatible with Hughes-Liu elements. Second, it behaves

similarly to the Rate Sensitive Power Law Plasticity model while still able to account for strain-rate effects.

Belytschko-Schwer elements were used with the Plastic-Kinematic material model. This model differs from both Power Law Plasticity models in how it shows behavior after yielding. Instead of using an exponential equation to describe post-yield behavior, it uses a linear representation.

Finally, both Hughes-Liu and Belytschko-Schwer elements are compatible with the elastic material model, which is typically the material type used for cladding elements in detailed fuel assembly models. Elastic materials are accurate up to the point of yield, so it is typical to define the failure criteria at the yield strength, which is conservative.

2.2.1 Rate Sensitive Power Law Plasticity

The Rate Sensitive Power Law Plasticity (*MAT_064) material model is ideal to use for this analysis because of its sensitivity to strain rate, which is present in the fuel cladding material. Table 2-2 shows the inputs required by the Rate Sensitive Power Law Plasticity model (as described in the software documentation).

Table 2-2: Required inputs for the Rate Sensitivity Power Law Plasticity model.

k	87.97 x 10^3 psi	Material constant
m	0.015	Strain rate sensitivity exponent
n	0.127716	Hardening exponent
ε_0	0.006	Initial strain rate

The equation relating stress to strain is

$$\sigma_y = k\varepsilon^n \dot{\varepsilon}^m$$

As discussed in the previous section, this material property cannot be used with either Hughes-Liu or Belytschko-Schwer element formulations; therefore, the experimental data collected in this format must be converted to an alternate material model. The next two sections describe this material data conversion.

2.2.2 Power Law Plasticity/Hughes-Liu

To accommodate the Hughes-Liu element formulation, the Power Law Plasticity (*MAT_018) material model will be used:

$$\sigma = \left[1 + \left(\frac{\dot{\varepsilon}}{C}\right)^{\frac{1}{P}}\right] k\left[\varepsilon_e + \varepsilon_{eff}^P\right]^n$$

Table 2-3: Inputs required for the Power Law Plasticity/Hughes-Liu analysis.

k	87.97 x 10^3 psi	Strength coefficient
n	0.127716	Hardening exponent
C	-7.75 x 10^{-4}	Strain rate parameter
P	1	Strain rate parameter

The power law constants must be set so that the material model matches realistic behavior when using constants derived from experiment. Because this experiment was designed to produce constants that happen to match the rate sensitive power law plasticity constants, the power law material model must use values for C and P that will mimic rate sensitive power law plasticity. Therefore, the following equation must be satisfied (where power law plasticity is shown on the left, and rate sensitive power law plasticity is on the right):

$$\left[1+\left(\frac{\dot{\varepsilon}}{C}\right)^{\frac{1}{P}}\right] k\left[\varepsilon_e+\varepsilon_{eff}^{P}\right]^n = k\varepsilon^n\dot{\varepsilon}^m$$

The justification for the values for C and P are given below.

Given: Data in the form of Rate Sensitive Power Law Plasticity, which is

$$\sigma = K\varepsilon^n\left(\dot{\varepsilon}\right)^m$$

Goal: Determine which parameters C, P, and n (hardening exponent) will cause the relationship between stress and strain for power law plasticity to equal that of rate sensitive power law plasticity, or

$$K\varepsilon^n\left(\dot{\varepsilon}\right)^m = \left[1+\left(\frac{\dot{\varepsilon}}{C}\right)^{\frac{1}{P}}\right] K\left(\varepsilon_e+\varepsilon_{eff}\right)^n$$

Understanding that the following are equivalent,

$$K\varepsilon^n = K\left(\varepsilon_e+\varepsilon_{eff}\right)^n$$

all that remains is to set values for C and P such that

$$\left(\dot{\varepsilon}\right)^m = \left[1+\left(\frac{\dot{\varepsilon}}{C}\right)^{\frac{1}{P}}\right]$$

Values for C and P are selected and make the previous equation true. For simplicity, this study assumes a fixed strain rate of 0.0001 and chooses a strain hardening exponent of 0.015, which comes from the experimental data (see Table 2-1). With these assumptions, there is freedom to define either P or C independently. In this study, P is set to 1, which allows C to be calculated as follows:

If $P = 1$, $\dot{\varepsilon} = .0001$, and $m = 0.015$, then

$$C = \frac{\dot{\varepsilon}}{\dot{\varepsilon}^m - 1} = \frac{.0001}{(.0001)^{0.015} - 1} = -7.75 \times 10^{-4}$$

Using values of C=-0.00075 and P=1 cause the power law plasticity relationship to mimic the behavior of rate sensitive power law plasticity for this set of assumptions.

Note that this material was derived for use in a quasi-static load case to test model behavior against a static closed form solution. When the strain rate is variable, P and C need to be chosen to provide a best fit to experimental data in the strain rate range of interest. Even though the structure of the Power Law Plasticity model is not the same as the Rate Sensitive Power Law Plasticity model, the P and C parameters are expected to provide enough freedom to match realistic strain-rate behavior over a desired range of strain rates. Choosing P and C can be treated as an optimization problem and can use the same kind of numerical methods to find the optimal P and C for a family of strain-rate-dependent material test data. This is recommended as a topic for future study.

2.2.3 Plastic-Kinematic/Belytschko-Schwer

This section describes the finite element model setup for Belytschko-Schwer beam elements used with the Plastic-Kinematic (*MAT_003) material model. The material model for Plastic-Kinematic behavior is described by the following relationship (from *LS-DYNA Manual*, R7.0, volume 2 [LSTC 2013]):

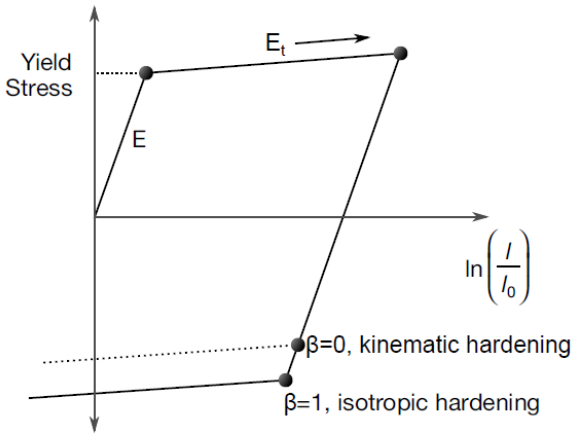

Figure 2-1: LS-DYNA Plastic-Kinematic material model stress-strain curve.

This material also scales the yield stress by the factor:

$$1+\left(\frac{\dot{\varepsilon}}{C}\right)^{\frac{1}{P}}$$

The same values used for C and P in the Power Law Plasticity/Hughes-Liu section are used in this analysis for the same reasons.

The values used for the analysis variables are shown in Table 2-4.

Table 2-4: Required inputs for the Plastic-Kinematic model.

ρ	0.518 x 10^{-3} lbf-s^2/in	Mass density
E	9.93 x 10^6 psi	Young's modulus
E_t	0.874 x 10^6 psi	Tangent modulus
ν	.36	Poisson's ratio
P	-7.75 x 10^{-4}	Strain rate parameter
C	1	Strain rate parameter
β	0	Hardening parameter

2.3 Results: Finite Element Analysis and Theory Comparison

Each horizontally-oriented beam segment model was loaded at one end with a downward vertical force in a quasi-static analysis. The force was applied in a stepwise manner, and the duration of the analysis was long enough that the beam settled into a deformed shape. The figures shown in this section report values for maximum moment and stress in the beam in terms of percent error. Percent error has been determined using the following:

$$\%\,Error = \frac{Theoretical\_Value - FEA\_Value}{Theoretical\_Value} \cdot 100$$

Early in the analysis of the results, it became clear that the value used for shear factor had very little effect on the accuracy of the results. The three values for shear factor, 0.3, 0.8, and 1.3, were used for each of the four quadrature rules, both material models, and both beam element formulations, under a load of 15 and 30 pounds. The choice of 15 and 30 pounds was used to give results well within the elastic range (15 lbs) and just barely into the plastic range (30 lbs). Additionally, some results show a 50-pound load, which was used to simulate loading well into the plastic range. The purpose of the 50-pound load case is to investigate the model behavior. Because the closed form solution assumes elastic behavior, the reported error takes on a different meaning. In the 50-pound load cases, the error represents the difference between elastic and plastic cladding behavior.

Figure 2-2 uses three separate lines for the three different shear factors, which are all overlaid. This figure graphically shows that shear factor has a very small influence on the results, independent of the material model or element formulation used.

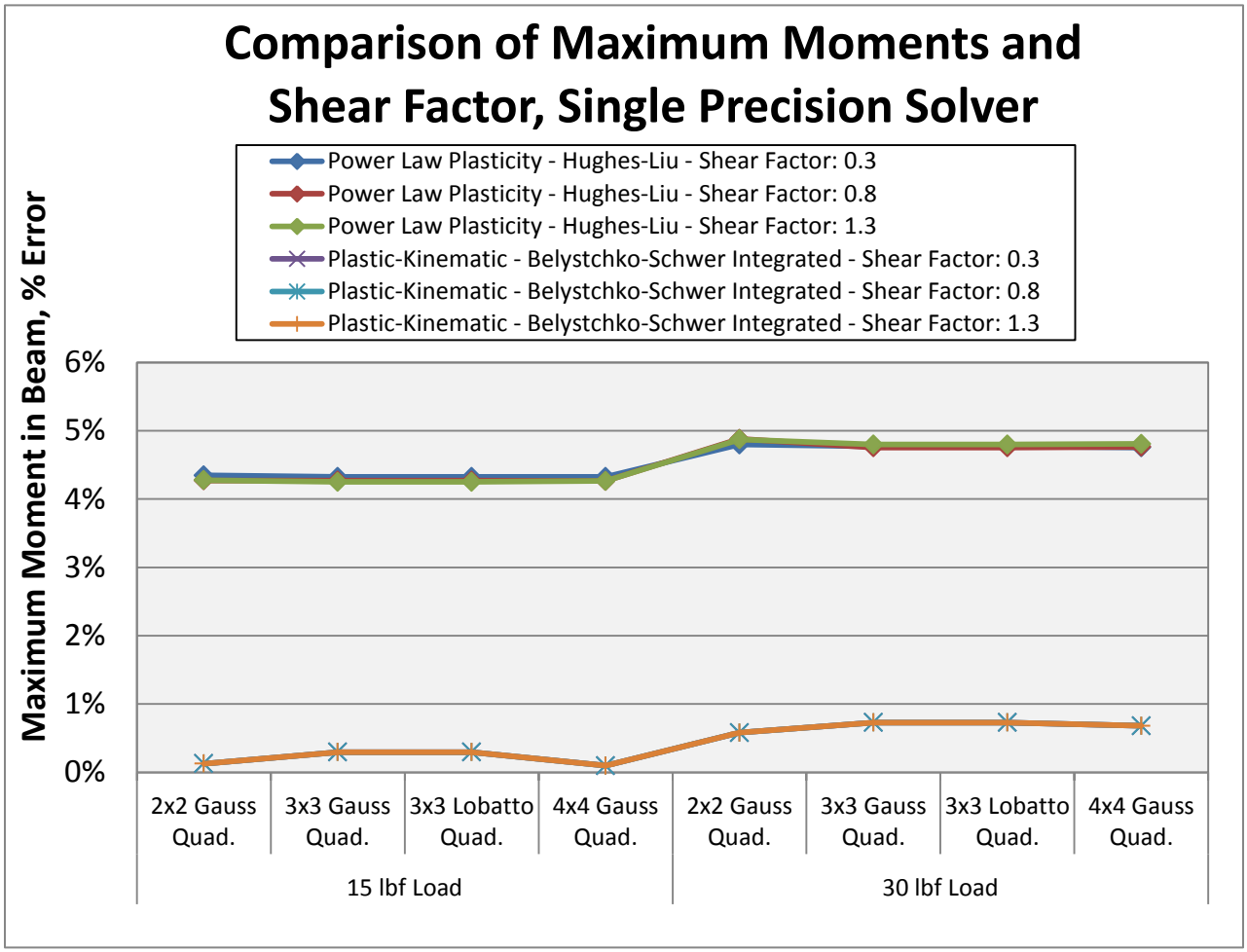

Figure 2-2: Three different shear factors, indicated by three overlaid lines, indicate that shear factor has very little influence on results.

Quadrature rule can have an effect on analysis accuracy. In some cases, such as in the maximum beam stress, using 2x2 Gauss Quadrature was extremely inaccurate. In all other cases, it was either comparable or had slightly worse results. Therefore, it is recommended to not use this quadrature rule, as illustrated in Figure 2-3.

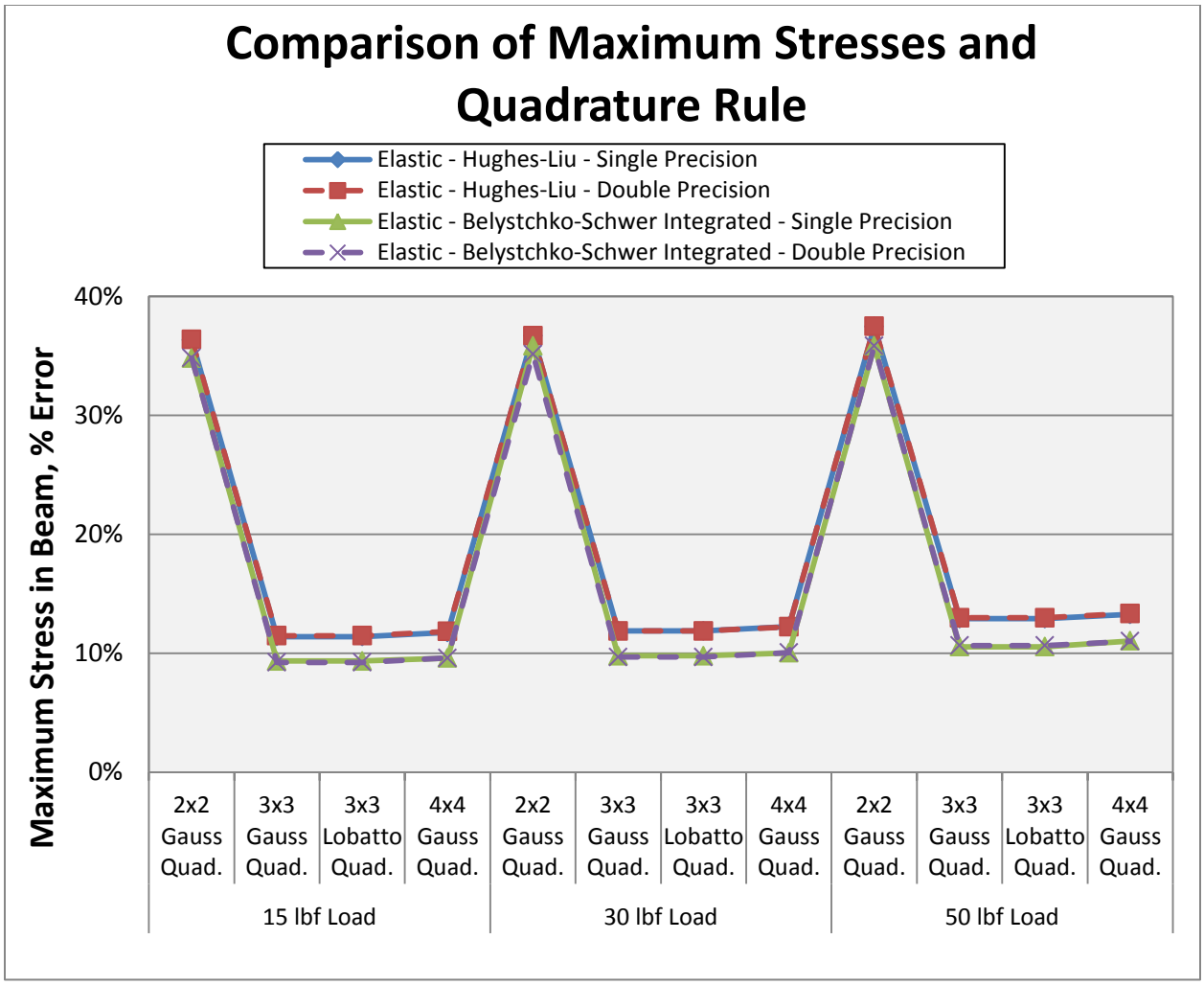

Figure 2-3: Results comparison study done to determine viable quadrature rule selection.

The element formulation parameter has the greatest effect on model accuracy. However, because the element formulations must correspond to certain material models, the two parameters' effects cannot be disassociated from each other when using plastic material models. Therefore, this combination can be considered as one parameter. Figure 2-4 shows that the most accurate element formulation is the Belytschko-Schwer integrated beam. It also shows that the elastic material model results in the least amount of error when compared to theoretical values of maximum moment.

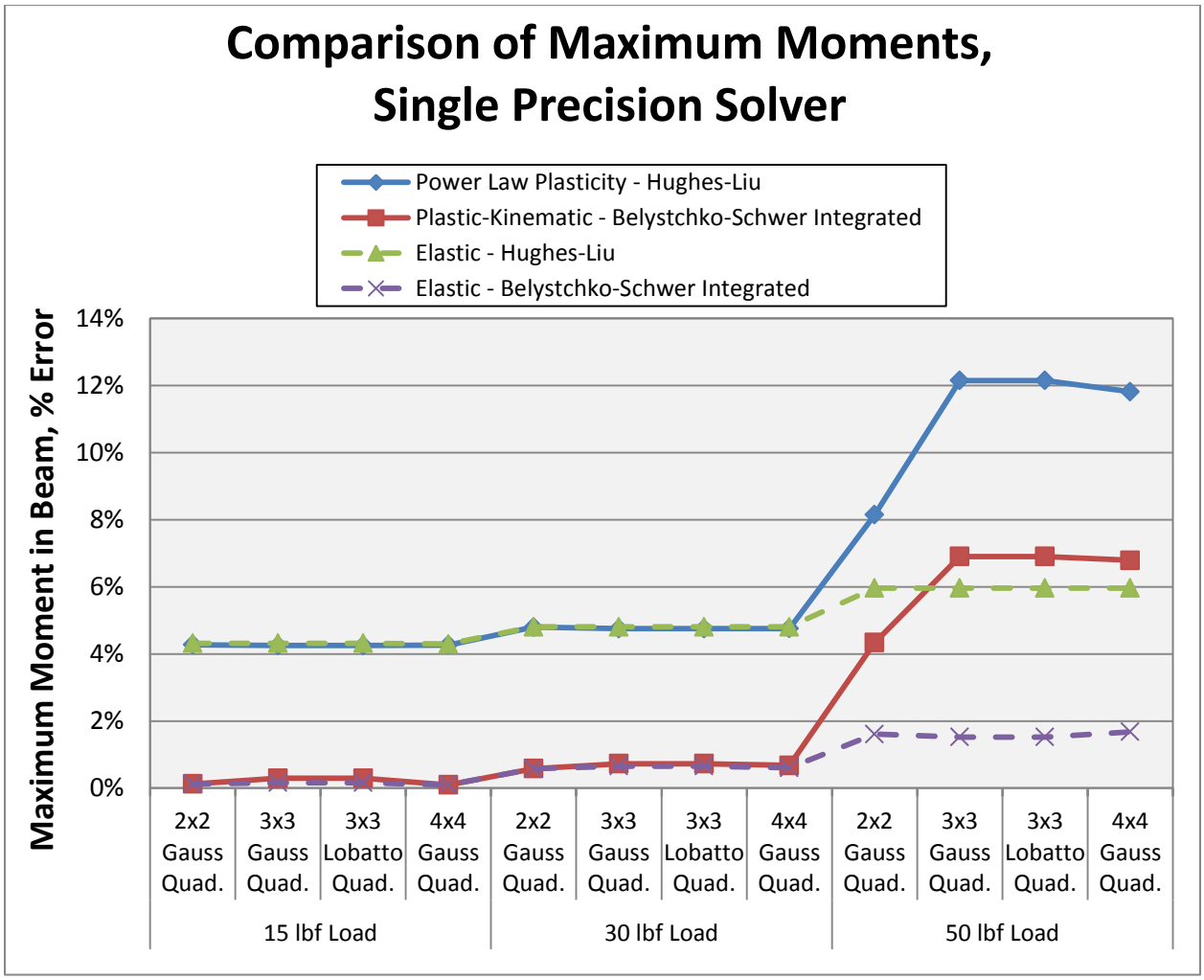

Figure 2-4: Results comparison showing the maximum moments compared across multiple element formulations, material models, quadrature rules, and loads. The comparison is done using a single precision LS-DYNA solver.

The reason for this apparent sharp increase in error seen in the two plastic material models at 50 pounds is due to the behavior of these models after material yield. Because the error is reported with respect to ideal, elastic behavior, the plastic material models should be expected to deviate from this value. The difference in results at 50-pound load is more an indication of the difference between the elastic material model and the plastic material model in the plastic deformation range than an indication of error.

The reason for using the elastic material model as the most suitable model is that it gives identical results as the more time expensive plastic models in the pre-yield regime. Because element failure is determined by whether the material has reached its yield point, post-yield behavior is irrelevant. Therefore, it makes the most sense to use the material model that saves the most time during analysis.

Next, the most accurate set of analyses was run using the double-precision LS-DYNA solver. This step was done to determine whether using the more precise solver, which takes longer to solve, will generate more accurate results. As Figure 2-5 shows, the double-precision and single-precision solver yielded very similar results.

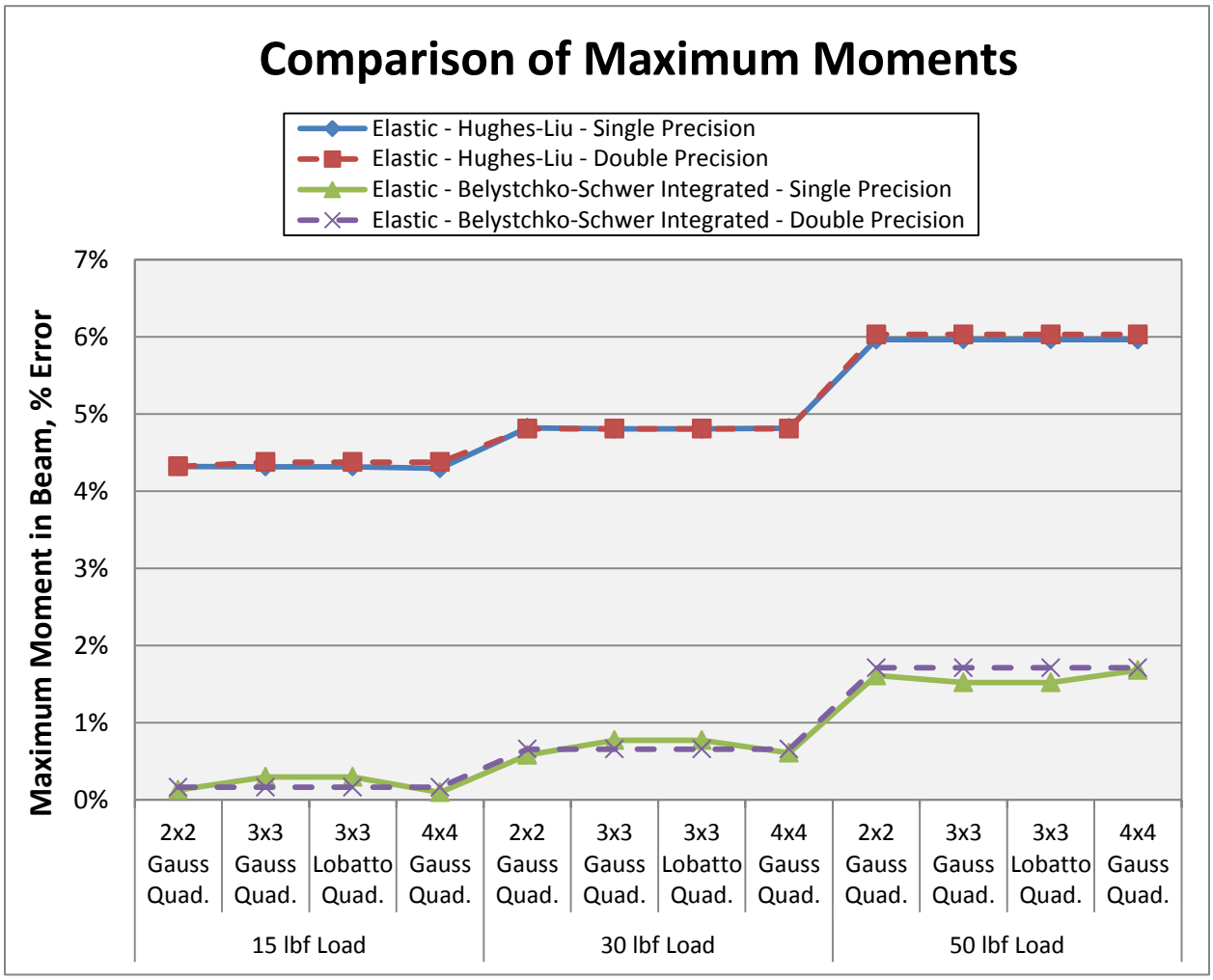

Figure 2-5: Results comparison showing the maximum moments compared across multiple element formulations, quadrature rules, loads, and the solver's precision using the most accurate material model found in earlier analyses (elastic).

Finally, the most accurate parameters were run again, except that this time the rod was modeled as a solid, circular beam element. The goal was to use the solid beam element to simulate a tubular rod. To do this, the elastic modulus was adjusted to change the value of E·I in the solid element to match the product of E·I from a tubular element. The values used are shown below and depicted in Figure 2-6.

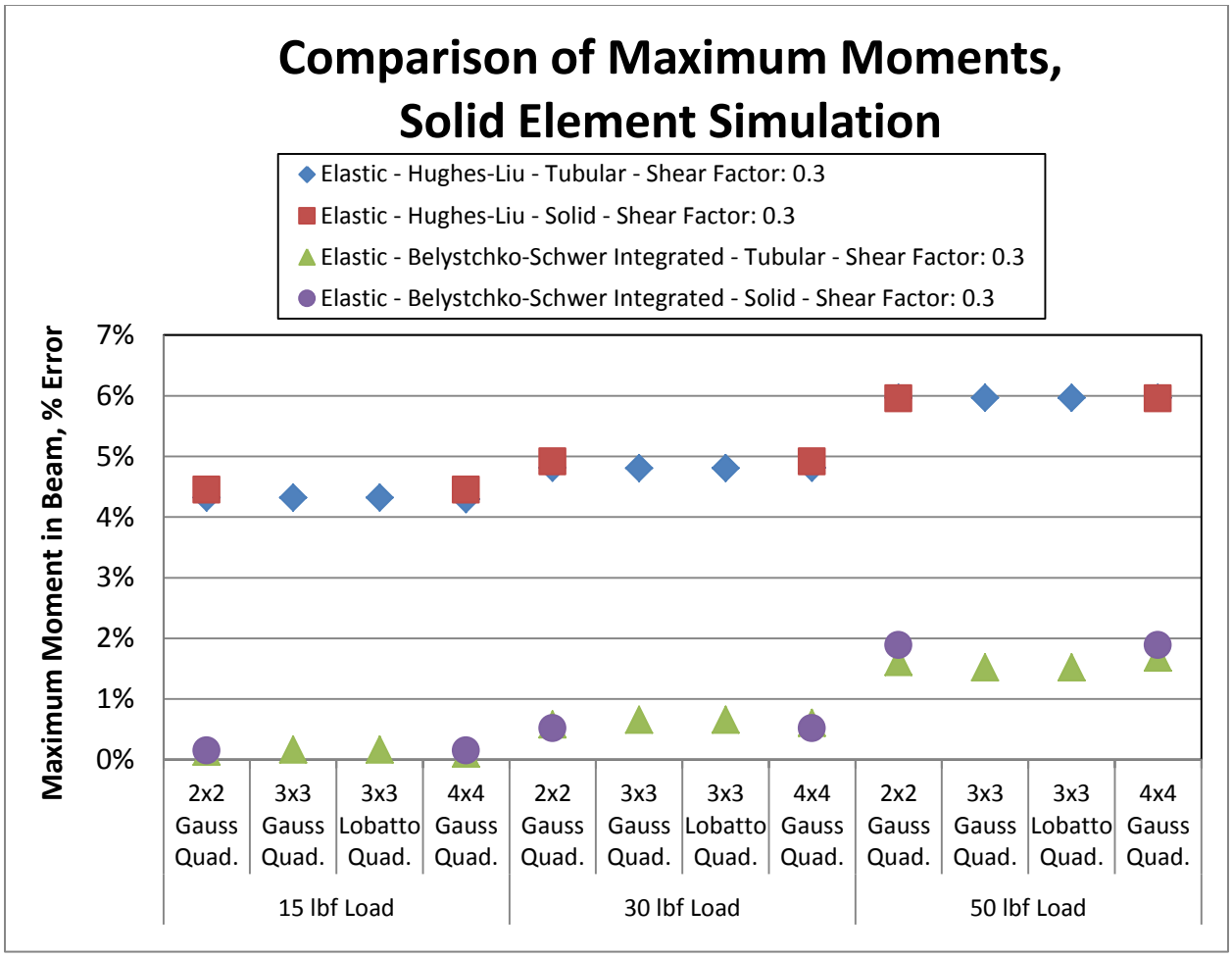

Figure 2-6: Most accurate set of analysis parameters re-run using a solid element formulation(not the hollow tube formulation from before).

$$E_{Actual} = 9.93 \times 10^{6}$$

$$I_{Tubular} = \frac{\pi\left(d_0^4 - d_i^4\right)}{64} = 3.412 \times 10^{-4} in^4$$

$$I_{Solid} = \frac{\pi\left(d_0^4\right)}{64} = 8.245 \times 10^{-4} in^4$$

$$E_{Actual} \cdot I_{Tubular} = 3.388 \times 10^{3} lb \cdot in^2 \text{S}$$

$$E_{Adjusted} = \frac{E_{Actual} \cdot I_{Tubular}}{I_{Solid}} = 4.109 \times 10^{6}\ psi$$

2.4 Conclusions and Future Work

The current study considered a section of cladding that was loaded in bending in the elastic and plastic cladding response range. It also investigated how to take standard strain-rate-dependent material test data and convert it into LS-DYNA material model format. The following conclusions can be made:

- Cladding analytical uncertainty: The typical PNNL detailed assembly models used the default beam element settings. Based on this study of cladding modeling options, the analytical uncertainty on the bending moment is in the range of ±5% for loads up to the cladding yield. Using higher element formulations can potentially reduce this range to ±1%.
- Cladding stress interpretation: This study demonstrates that the way LS-DYNA computes and records beam element stresses is not well suited to evaluating the cladding response. The error in element stresses can be ±40% for low element formulations and ±10% for high element formulations. This finding demonstrates that PNNL's typical post-processing approach, which uses a MATLAB script to combine element resultant bending moments and axial force, is more accurate than using integration point stresses.
- Best modeling options: The Belytschko-Schwer integrated beam element formulation with 4x4 Gauss quadrature and elastic material provided the best match to the elastic closed-form solution. A shear factor of 0.3 offered the best match, but shear factor was not a major factor in the accuracy. These are the best element options for loading conditions up to the material yield limit; when stresses above the cladding yield strength are expected, more evaluation is needed to determine the best modeling options.

Additional topics remain to be investigated:

- Validation of the plastic, strain-rate-sensitive cladding material model to other load scenarios: The cladding material models and beam element formulations were tested in a single bending load case. Additional closed-form solutions are available for study and can be used to determine error bands and quantify the analytical uncertainty associated with this kind of model. The PNNL cladding test data also provides experimental validation data for unirradiated fuel in tension, compression, and burst (from internal pressure) load cases.
- Best modeling options in plastic range: Additional study is needed to determine the best options for modeling when the cladding is expected to experience high plastic strains. This study demonstrates the ability to match elastic beam-bending, closed-form solutions, which covers most of the range of interest for cladding modeling. Additional investigation is needed to be able to accurately model cases with cladding in the plastic response range. Used fuel has some available ductility, in the range of 1-2% plastic strain, and it would be ideal to have cladding models that behave like realistic used fuel and accurately predict cladding failure.
- Develop a method for determining variable strain-rate material parameters: Determining the C and P parameters for variable strain-rate material behavior is an optimization problem. PNNL testing has provided some test data on the strain-rate behavior of non-irradiated zirconium alloys, but the strain-rate sensitivity is relatively low and is potentially insignificant. If the UFDC program can get irradiated cladding data (such as tensile data collected at a number of strain rates between 0.0001 and 100), then the LS-DYNA cladding material models can be tuned to match by determining optimal C and P parameters.

3.0 CLADDING THINNING UPDATE

One important goal of the Structural Uncertainty task is to be able to estimate how much material degradation is needed to cause failure in the components of a DSC system under expected loading conditions to help material researchers determine which material degradation processes are worth studying. This work is intended to help the UFDC prioritize the material testing programs.

The Structural Uncertainty task considers three load cases on a vertical DSC system: tip-over of the vertical DSC onto a concrete pad surface, a handling drop of the MPC into the DSC during loading or unloading, and a seismic loading of the DSC while it is sitting on a concrete pad. Last fiscal year, all three load cases were evaluated with a detailed fuel assembly model that used the default beam formulation. This fiscal year, the tip-over case was selected to be upgraded with the most accurate beam element properties determined in the previous section. The goal was to determine the amount of margin on the fuel cladding, and then run cases with the cladding artificially thinned by an amount that would lead to cladding failure.

As this modeling effort progressed, it became apparent that the upgraded beam element formulation led to predictions of cladding failure before any thinning was applied to the cladding. Three different element formulations were tested, and each one predicts widespread cladding failure, while the results from last fiscal year predicted zero cladding failures using the default beam element formulation. This work is still in progress at the time of this writing, and a better understanding in the difference in cladding response between the default and optimal beam formulation settings is needed. The authors have not ruled out the possibility that a modeling error is responsible for the unusual shift in predicted cladding response. The preliminary results of this study are presented briefly and are expected to be finalized in FY16.

One accomplishment for this fiscal year was the creation of a new process for visualizing the location of highly stressed cladding elements, which is used in Figure 3-1, Figure 3-2, and Figure 3-3. Because the cladding stress is calculated outside LS-PREPOST, visualization of the location of high-stress cladding elements has been difficult. This new method will likely become the standard way to illustrate high-stress cladding elements for the detailed fuel assembly model.

3.1 Overview

This is an ongoing modeling task, and what is reported here represents the state of the work at the end of the current fiscal year. This task is intended to continue in FY16. The tip-over model described in Klymyshyn 2014a was modified to have a more accurate beam element formulation, based on the work described in Section 2.0. The beam element formulations were changed as detailed below and the beam post-processing routine was altered to consider bending moments in two orthogonal directions. The main difference between the current results and FY14 results was the calculation of much higher bending moments in the current model results. This difference could be due to the change in element formulation, but the bending moments are much higher than the ±5% that was witnessed in the comparisons to closed-form solutions in Section 2.3. This is an indication that something else may be driving the difference in calculated response, such as

a contact definition problem or a numerical error of some kind. The issues with the tip-over model are expected to be resolved early in FY16.

3.1.1 Element Formulation

The element formulations for the three analyses (Analysis 1, Analysis 2, and Analysis 3) are as shown here. Each of the analyses used the elastic material model. The LS-DYNA inputs for the three analyses are described in Table 3-1.

Table 3-1: Finite element model parameters.

	Element Formulation	Shear Factor	Quadrature Rule	Cross-section Type	Element OD (m)
Analysis 1	Belytschko-Schwer full cross-section integration	1.0	4x4 Gauss	Tubular	0.009144
Analysis 2	Belytschko-Schwer tubular beam with cross-section integration	0.3	2x2 Gauss	Tubular	0.009144
Analysis 3 (optimal formulation)	Belytschko-Schwer tubular beam with cross-section integration	0.3	4x4 Gauss	Tubular	0.009144

3.2 Results

The locations of the 75 elements with the highest cladding stress are graphically shown in Sections 3.2.1, 3.2.2, and 3.2.3 below. The results for Analysis 3, which used elements expected to be most accurate, are tabulated in Section 3.2.3, Table 3-2. Each of the three element formulations shows results that far exceed both yield stress and ultimate tensile strain for Zircaloy-4. These values for stress and, more importantly, bending moments exceed what is expected from this analysis based on the previous work done in 2014. These results should be considered preliminary and are likely to be revised when the work is finalized in FY16.

3.2.1 Analysis 1 Results

The maximum stress found in the fuel rods occurs at the location shown with the red “X” below. The stress in this element occurred at 0.118 seconds, or 0.100 seconds after impact. The stress in this element at this time is 3.1 GPa. 16,452 of 31,944 elements exceeded both the yield and ultimate tensile stress at some time in the analysis.

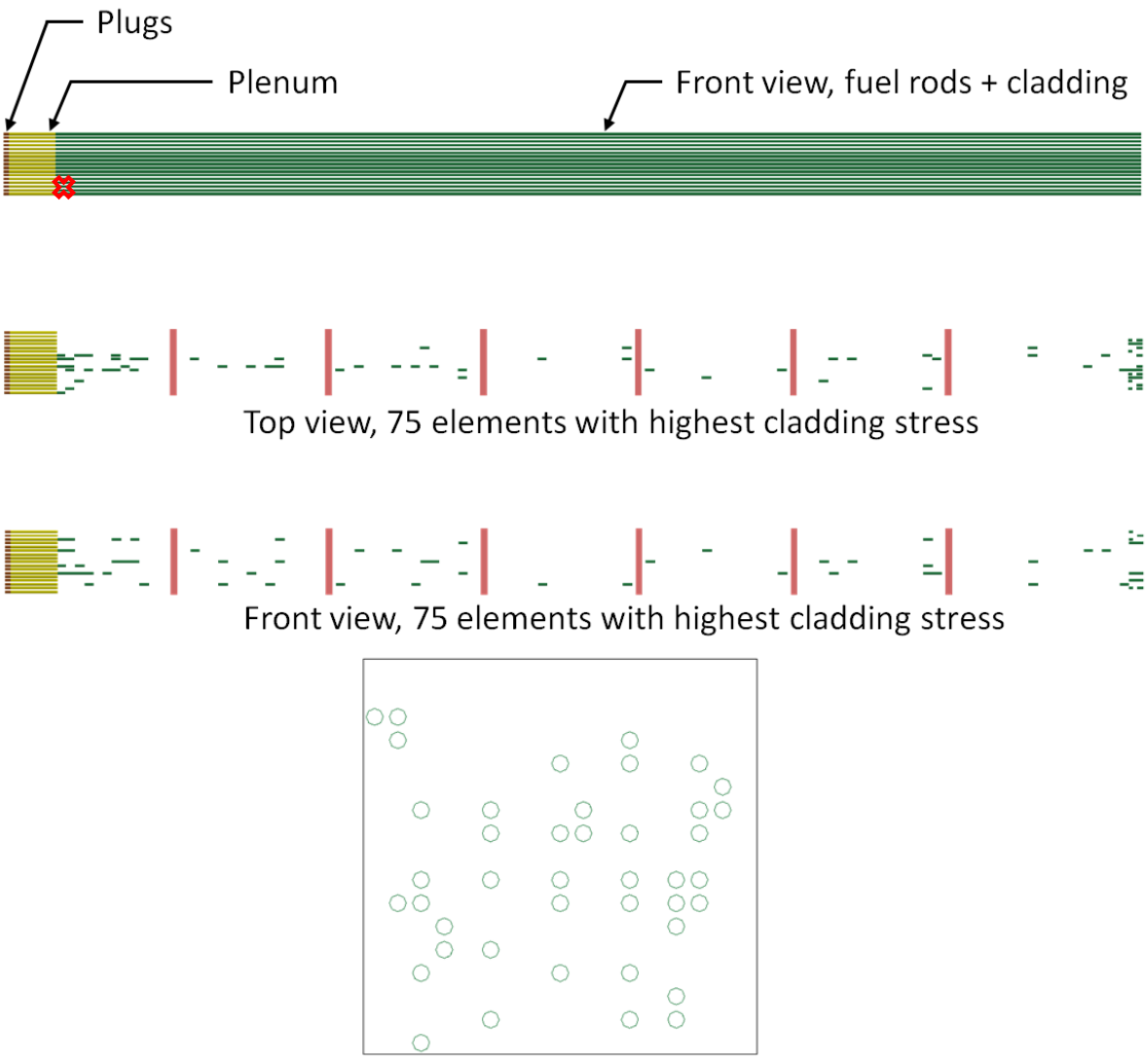

Figure 3-1: Graphical representation of element failure locations for Analysis 1.

3.2.2 Analysis 2 Results

The maximum stress found in the fuel rods occurs at the location shown with the red "X" below. The stress in this element occurred at 0.094 seconds, or 0.076 seconds after impact. The stress in this element at this time is 3.61 GPa. 14,776 of 31,944 elements exceeded both the yield and ultimate tensile stress at some time in the analysis.

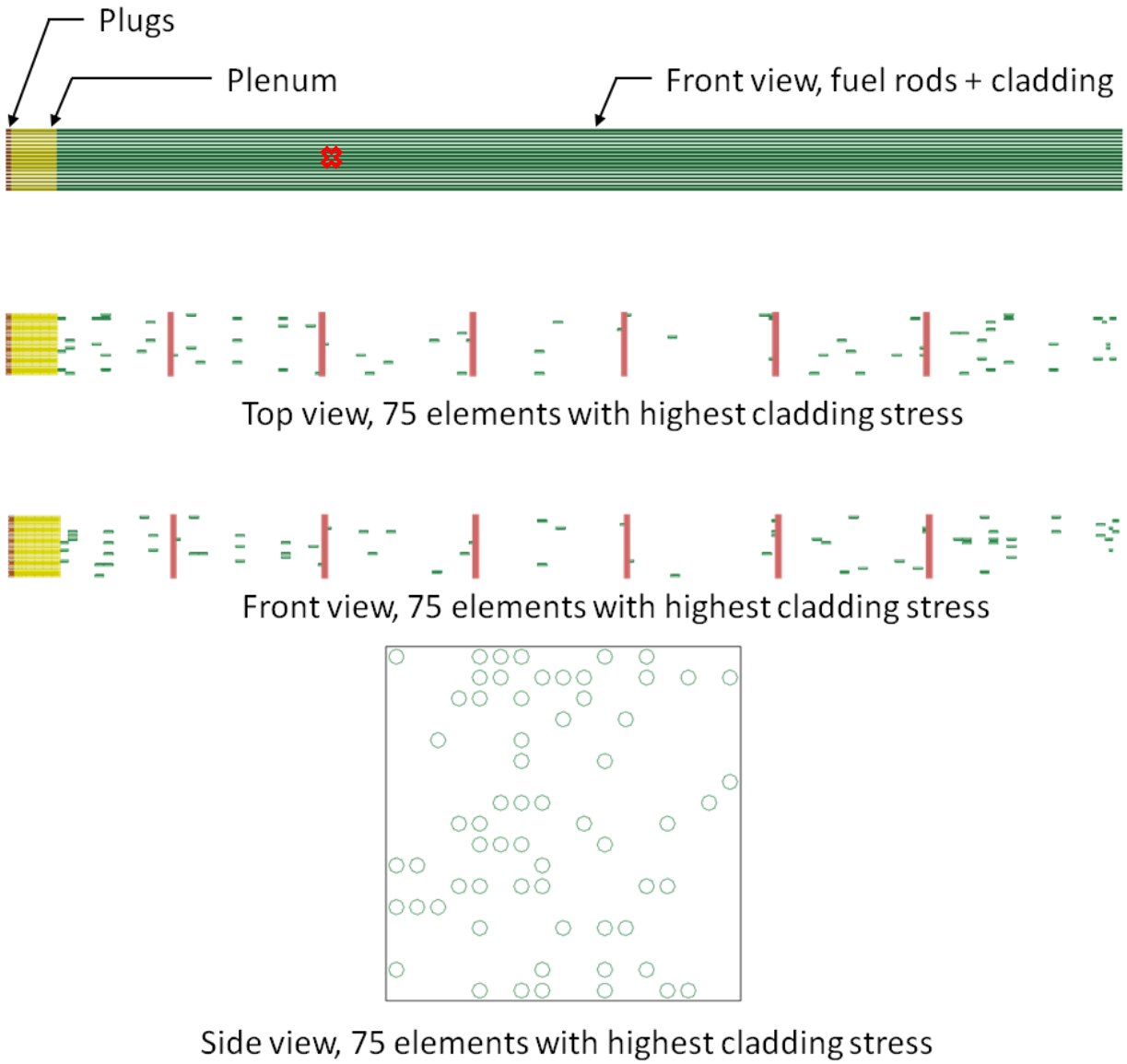

Figure 3-2: Graphical representation of element failure locations for Analysis 2.

3.2.3 Analysis 3 Results

The maximum stress found in the fuel rods occurs at the location shown with the red "X" below. The stress in this element occurred at 0.148 seconds, or 0.130 seconds after impact. The stress in this element at this time is 2.84 GPa. 13,808 of 31,944 elements exceeded both the yield and ultimate tensile stress at some time in the analysis.

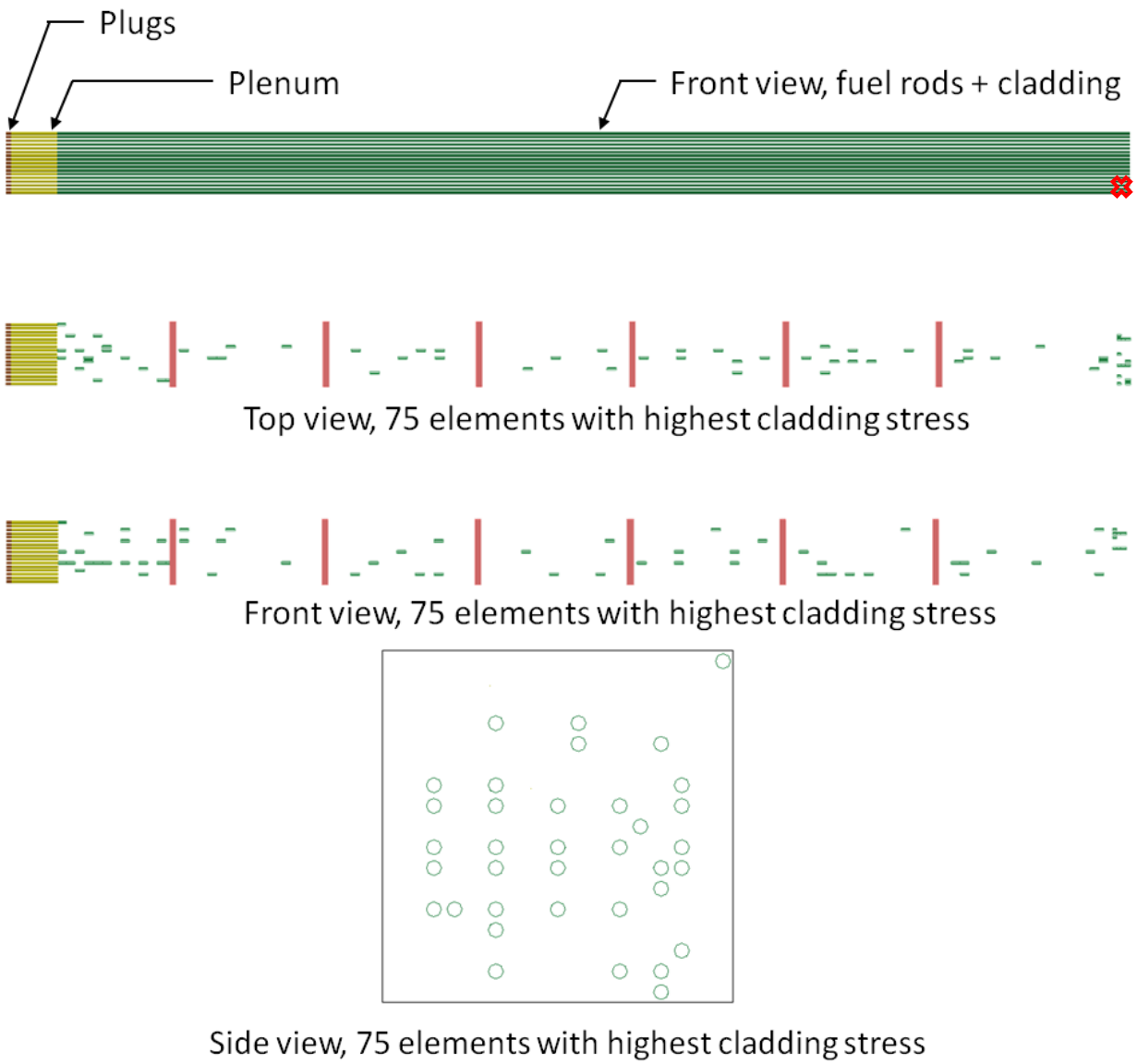

Figure 3-3: Graphical representation of element failure locations for Analysis 3.

Table 3-2: Analysis 3 results, showing peak cladding strains and stresses.

Cladding-Strain	Time [sec]	Element #	F_axial [N]	Moment-S [N-m]	Moment-T [N-m]	Cladding-Stress [Pa]
0.031	0.148	102750	-63.63	86.56	2.02	2.844E+09
0.030	0.092	119309	-93.26	83.64	8.52	2.759E+09
0.029	0.076	119309	189.92	78.12	9.00	2.599E+09
0.028	0.084	119325	481.43	-76.59	-8.11	2.565E+09
0.026	0.062	123828	815.01	-69.90	-0.34	2.354E+09
0.024	0.124	119309	414.01	-66.19	-3.37	2.208E+09
0.024	0.156	142530	338.54	-65.77	-2.86	2.188E+09
0.024	0.088	119309	-96.34	-66.32	-2.97	2.177E+09
0.024	0.134	119325	-379.42	-66.79	-4.26	2.176E+09
0.024	0.106	134351	211.15	-64.43	-2.93	2.136E+09
0.023	0.082	119325	-607.74	65.36	5.74	2.118E+09
0.023	0.166	122853	-1339.07	-66.99	-0.95	2.115E+09
0.023	0.132	115089	-499.84	65.03	-1.15	2.106E+09
0.023	0.148	111158	-927.56	65.33	5.95	2.096E+09
0.023	0.084	122640	434.48	62.36	7.41	2.095E+09
0.023	0.184	119325	8.74	-62.99	-3.84	2.076E+09
0.023	0.156	119309	-239.01	-63.04	-6.19	2.067E+09
0.023	0.136	119325	-322.21	62.90	7.25	2.061E+09
0.023	0.166	102734	94.06	-60.75	-11.31	2.039E+09
0.022	0.196	125019	-278.92	62.43	1.77	2.036E+09

3.3 Conclusions and Future Work

This work is still ongoing at the end of this fiscal year. Because the cladding stresses are so much higher than predicted in 2014 when the only change to the model is supposed to be upgraded beam element formulations, the results are suspicious and need to be carefully reviewed before they can be considered final. Because of the uncertain nature of the results, it is premature to draw any conclusions at this time.

The following activities are recommended for FY16 for the cladding thinning study:

- Complete the modeling review of the tip-over case: Additional model review steps are necessary to confirm that the results described in this progress report are valid. Basic quality assurance steps and model review were performed this fiscal year, but a deeper comparison to the FY14 results is needed. It may be necessary to test the models on different computer platforms and upgrade to LS-DYNA version 8.0.
- Upgrade the cladding in the handling drop and seismic load case models: The handling drop and seismic load cases predicted much lower cladding stresses than the tip-over load case, so there is still likely to be a stress margin on the cladding when the beam elements are upgraded. The cladding thinning study can continue as planned for those load cases, so the amount of cladding necessary to cause a failure can be quantified.

4.0 STRESS CORROSION CRACKING OF MPC

Extended dry storage of used nuclear fuel presents a number of technical challenges, one of which is predicting the sealing performance of canisters throughout times that may extend to hundreds of years. Time-dependent processes such as SCC and other phenomena could affect the structural integrity of materials that compose the DSC system or its contents. This study addresses the effect of SCC on the leak integrity of canister seal welds in a hypothetical vertical DSC system.

4.1 Introduction

Klymyshyn et al. (2013) performed a detailed finite element analysis to predict the plastic deformation that may occur during tip-over of a generic multipurpose spent fuel canister. The analysis predicted that the maximum plastic strains in the seal weld were nearly equal to the minimum elongation of the stainless steel canister material. The current study extends the previous analysis to estimate the effect of SCC on the canister seal weld integrity. The original results were reviewed to estimate locations where wall thinning due to SCC would be the most damaging to the seal welds. The finite element analysis was then repeated with finite elements removed from the weld thickness to simulate the presence of a flaw in the worst-case locations. The predicted stress and strain results were re-evaluated to estimate if the likelihood of weld failure was increased. The analysis also considers the triaxiality of stresses during plastic deformation in assessing the local failure strains. The susceptibility of canister steels to SCC under a range of chemical and temperature and humidity conditions is summarized along with the level of SCC damage that may be expected. In addition, we present elastic-plastic fracture and plastic collapse analyses that show that even in the presence of cracking, plastic deformation of the ductile 304 stainless steel canister body is the expected failure mode rather than elastic-plastic fracture.

4.2 The Susceptibility of Canister Steels to Stress Corrosion Cracking

The U.S. Nuclear Regulatory Commission (NRC) has sponsored detailed studies on SCC of stainless steels used in dry storage containers. NUREG/CR-7030 (Caseres and Mintz 2010) studied SCC of 304 and 316 stainless steels in the presence of chloride salts (simulated sea salt, reagent grade sodium chloride, magnesium chloride, and natural sea salt collected near Corpus Christi, Texas). Both unwelded and welded U-bend specimens were held under high bending stress, sprayed with salt solution, allowed to dry, and exposed to controlled temperature and high-humidity conditions. Conditions that allowed the salt to deliquesce (form a brine solution on the sample) resulted in significant corrosion and SCC after 32 weeks (304 stainless) and 128 weeks (316 stainless).

NUREG/CR-7170 (He et al. 2013) presents the results of further exposure testing to better understand the NUREG/CR-7030 findings in light of other studies that report chloride-induced SCC at lower salt concentrations, lower humidity, higher temperature, and lower stress/strain conditions. NUREG/CR-7170 also tested for SCC with non-chloride salts, including ammonium

sulfate [$(NH_4)_2SO_4$], ammonium nitrate (NH_4NO_3), ammonium bisulfate (NH_4HSO_4), and fly ash leached in deionized water. No cracking was observed on specimens exposed to any of the non-chloride salts, even when the test humidity was above the deliquescence relative humidity.

The Electric Power Research Institute (EPRI) also sponsored research on SCC of stainless steels used in dry storage canisters. Enos et al. (2013) measured the chemistry of dust samples collected from canisters at the Calvert Cliffs interim storage facility. The chemical analysis showed the following:

- The dust was largely calcium sulfate, with chlorides present in only trace amounts.
- The sodium and chloride concentrations in the dust were low despite close proximity to Chesapeake Bay.
- The authors concluded that the dust was largely from inland sources.

Enos et al. (2013) point out that the test conditions used in the SCC testing programs may be very conservative. The test conditions may not represent field conditions for several reasons:

- Sea salt may not represent the dust on the container surfaces.
- Exchange with atmospheric gases was limited in the controlled experiments.
- Other components in the dust may either reduce or increase the corrosivity of deliquesced brines.

Enos et al. (2013) also present concentration maps of chemicals found in precipitation around the United States. These maps are from the National Atmospheric Deposition Program, National Trends Network (http://nadp.sws.uiuc.edu/data/NTN/). The National Atmospheric Deposition Program website also allows downloading the concentration data measured at specific locations. The chemicals measured include Calcium (Ca^{2+}), Magnesium (Mg), Potassium (K), Sodium (Na), Ammonium (NH_4^+), Nitrate (NO_3^-), Chlorine (Cl), and Sulphate (SO_4^{2+}). The pH is also listed in the database. This source provides information from which to estimate the composition of atmospheric contaminants at local regions in the United States.

In summary, the SCC experimental studies show that controlled temperature and humidity conditions can be achieved where 304 and 316 stainless steels will stress corrosion crack in the presence of chloride salts. However, the three studies reviewed do not identify that these specific conditions currently exist at any interim storage facilities. SCC did not occur at temperature and humidity conditions where salt will not deliquesce. In addition, the actual surface contaminants at real locations may not be the right chemistry to promote SCC.

The current study assumes that SCC has occurred and seeks to estimate the depth of SCC cracking that could jeopardize the integrity of the canister seal weld in a tip-over accident.

4.3 The Estimated Extent of Stress Corrosion Cracking

SCC occurs in the presence of tensile stress. The axial tensile stress at the outer surface of the top seal weld (the assumed crack initiation site) is the sum of the pressure stress plus the weld residual stress (σ_{resid}). It is assumed here that the weld residual stress is significantly higher than

the pressure stress such that the pressure stress can be ignored. Figure 4-1 shows an example weld residual stress distribution used in the SCC evaluation of the extremely low probability of rupture program (NRC and EPRI 2011). The residual stress distribution in Figure 4-1 is expressed as a third-order polynomial with distributions on the surface stress (σ_0), the depth in the wall where the stress reverses sign (x_c), and the stress on the back face (σ_f). The residual stress is self-equilibrating such that the area under the curve in Figure 4-2 must be zero. The maximum extent of the tensile stress zone (x_c) is one-half the wall thickness when the stress is balanced in tension and compression. Therefore, this study assumes that SCC has occurred to a depth equal to 50% of the wall thickness.

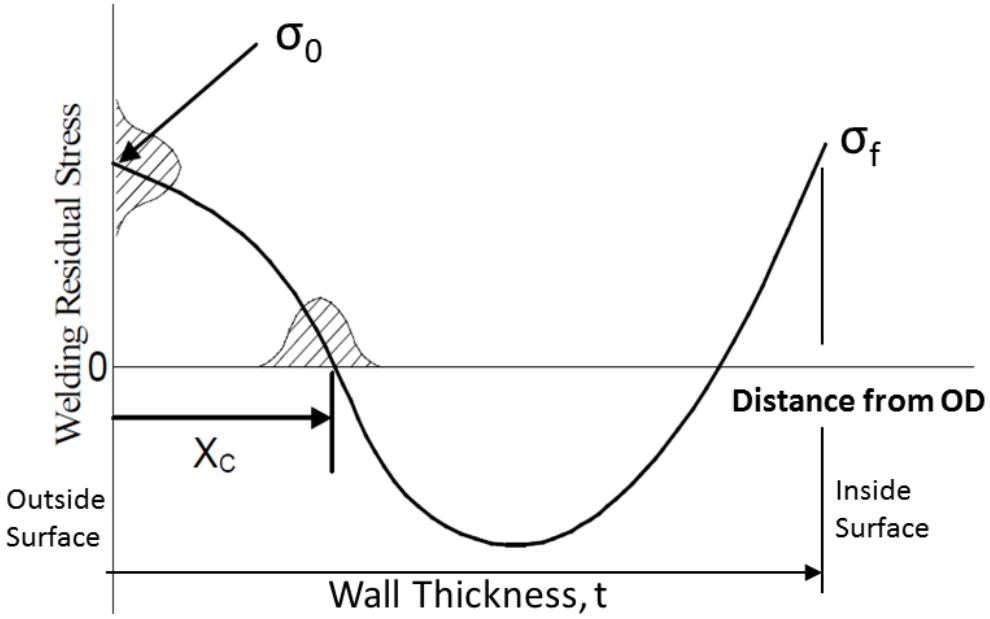

Figure 4-1: A representative distribution of weld residual stress(NRC and EPRI 2011).

4.4 The Effect of SCC on Predicted Canister Strains

Klymyshyn et al. (2013) performed a detailed finite element analysis of a generic multipurpose canister subjected to three off-normal conditions: 1) a tip-over accident, 2) a handling drop accident, and 3) seismic loads. Figure 4-2 illustrates the one-half symmetry impact model that was developed using the LS-DYNA software. The cylindrical canister body is constructed of bent plates so it can include both axial welds and intermediate circumferential welds. Circumferential welds connect the base plate to the canister body and provide the lid seal as well.

The tip-over accident was determined to be the most challenging to the canister seal welds. The LS-DYNA impact model estimated the maximum effective plastic strain to be 39% in the region of the top seal weld (Figure 4-3). Although this strain is near the tensile strain limit reported for 304 stainless steel (approximately 40%), it occurs at the impact zone in a state of hydrostatic compression. Under net compression, ductile materials tend to exhibit a higher strain to failure than the uniaxial failure strain. Conversely, triaxial stress states with significant net tension tend to reduce the effective plastic strain at which materials fail. Therefore, the previous analysis was further studied to consider the triaxiality of the stress tensor in adjusting the effective plastic

strains to identify areas of the seal weld where SCC would be most significant. A similar approach was used in the canister weld analysis documented in NUREG-1864 (Malliakos 2007). The current analysis extends the approach of NUREG-1864 by considering the effect of wall thinning due to SCC.

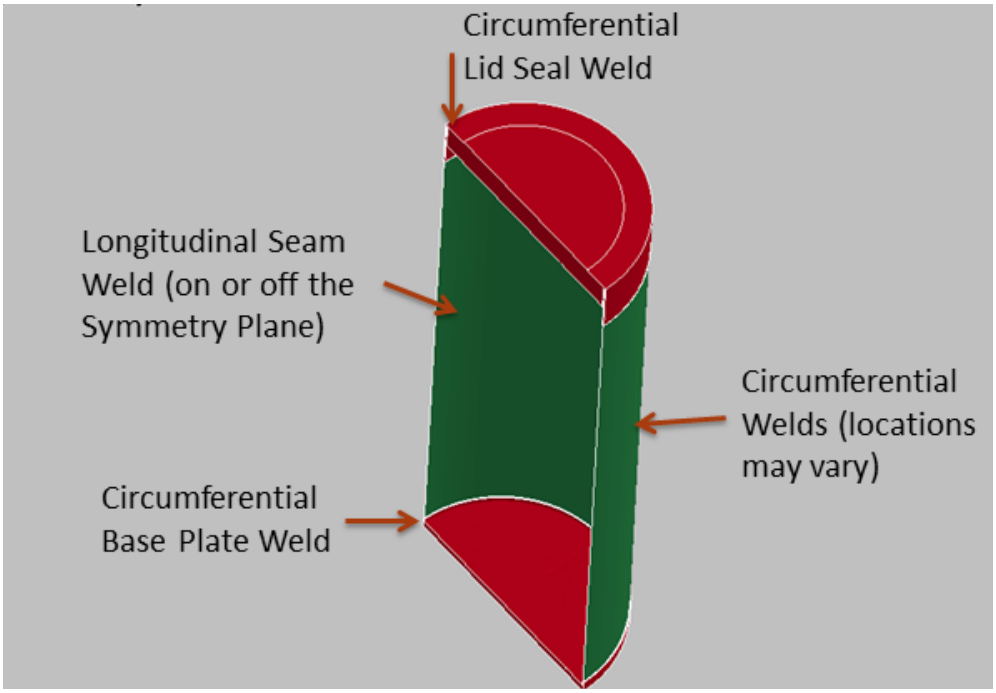

Figure 4-2: The half-symmetry canister impact model showing the weld locations.

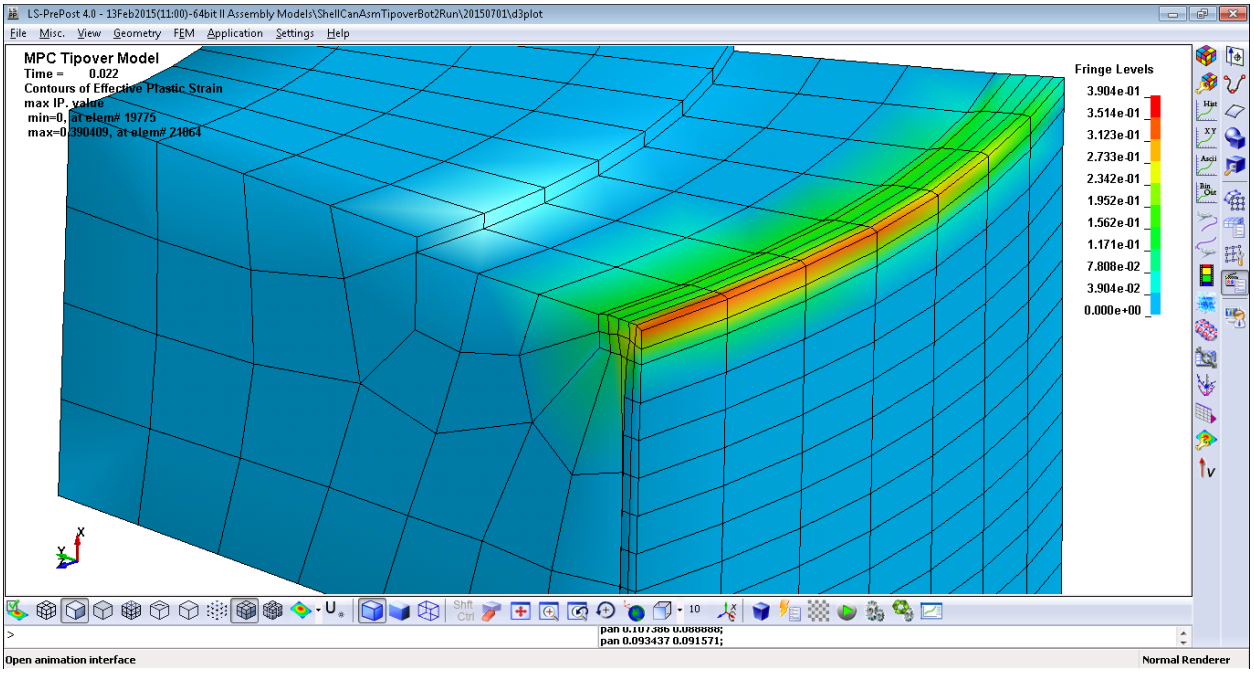

Figure 4-3: Effective plastic strain predicted in the tip-over impact evaluation (time = 0.022 seconds).

The triaxiality factor, *TF*, is defined as:

$$TF = \frac{\sigma_1 + \sigma_2 + \sigma_3}{\frac{1}{\sqrt{2}}\left[(\sigma_1 - \sigma_2)^2 + (\sigma_2 - \sigma_3)^2 + (\sigma_3 - \sigma_1)^2\right]^{1/2}} \quad (1)$$

where the numerator, $\sigma_1 + \sigma_2 + \sigma_3$, is the sum of the three principal stresses (3 times the hydrostatic stress), and the denominator is the effective stress. The triaxiality is evaluated during time steps when the rate of plastic deformation is the highest.

The ductility ratio, *DR*, is the ratio of the failure strain under combined stress divided by the uniaxial failure strain. Based on strain to failure tests of ductile materials under different stress combinations, Manjoine (1982) relates the ductility ratio to the triaxiality factor as:

$$DR = 2^{(1-TF)} \quad (2)$$

Figure 4-4 shows the ductility ratio vs. triaxiality for several materials under different stress combinations (Manjoine 1982). Note that the ductility ratio is truncated at a value of 2 for $TF \leq 0$.

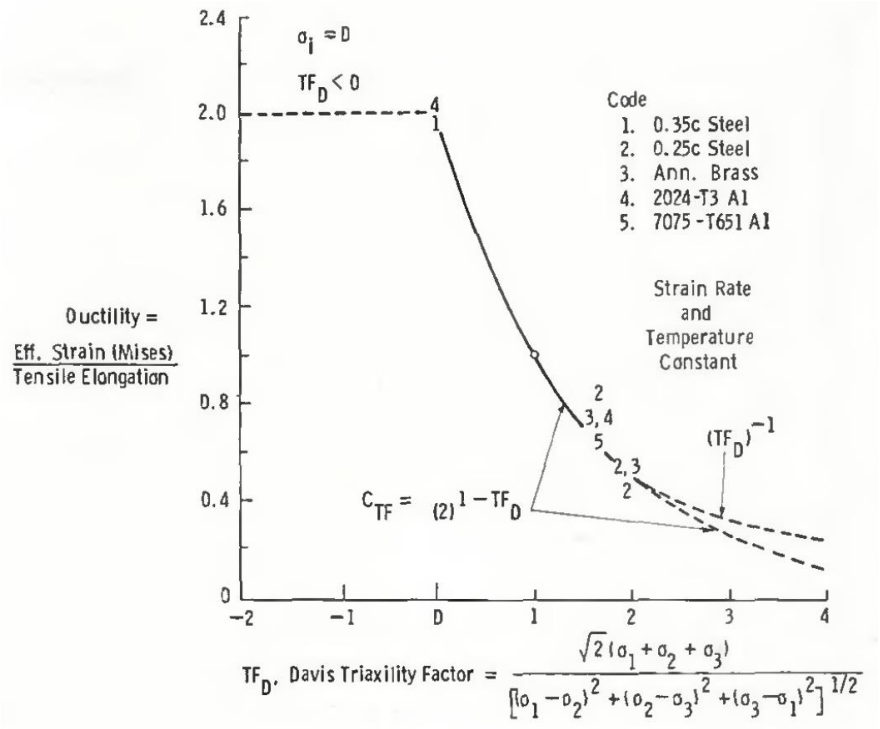

Figure 4-4: Ductility factor vs. stress triaxiality factor(Manjoine 1982).

Snow et al. (2009) present strain-based acceptance criteria under consideration by the American Society of Mechanical Engineers (ASME) for application to one-time, energy-limited events such as accidental drops and impacts. For locations at least three wall thicknesses away from a

local discontinuity, the maximum strain, ε_{max}, is limited to $\varepsilon_{\max} \le (0.67\,\varepsilon_{uniform})/TF$ where $\varepsilon_{uniform}$ is the strain at the onset of necking in a uniaxial tension test. For locations less than three wall thicknesses from a gross discontinuity, the strain limit is increased to $\varepsilon_{\max} \le (0.85\,\varepsilon_{uniform})/TF$. However, it is stipulated that these criteria do not apply to containment boundary fillet welds or partial penetration welds. Figure 4-5 compares the proposed strain criteria with the ductility factor for a range of triaxiality factors.

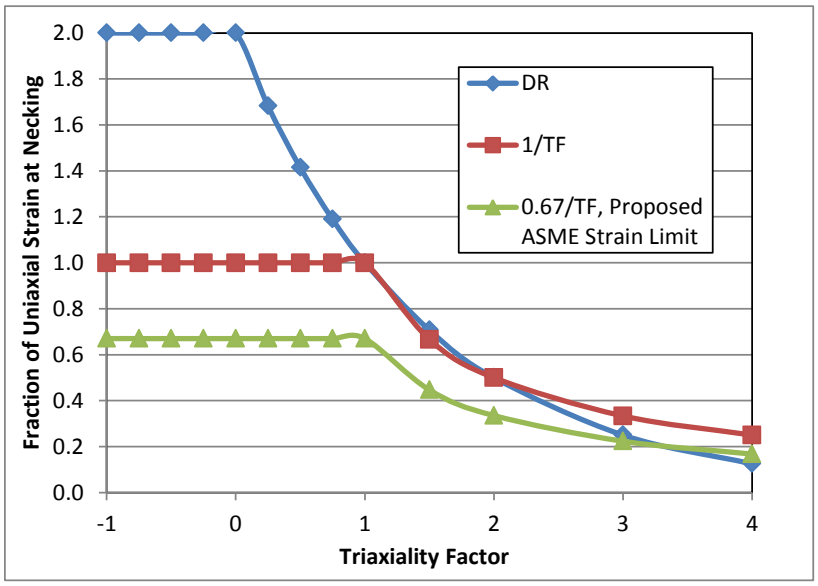

Figure 4-5: The ductility factor compared to 1/TF and the 0.67/TF limit proposed by Snow et al. (2009) for the ASME Code.

To identify locations in finite element analysis where the stress triaxiality reduces the strain to failure, one can divide the calculated effective plastic strains by the ductility ratio and compare the adjusted strain with the uniaxial tensile strain limit. Therefore, locations in the finite element model with 1/DR > 1 signal local stress combinations that reduce the margin between the calculated strain and the failure strain.

The LS-DYNA software includes a triaxiality output variable; however, it is defined as the hydrostatic stress divided by the effective stress, or TF/3. Figure 4-6 plots 1/DR vs. the LS-DYNA triaxiality. In evaluating the impact model results, we are looking for locations around the upper and lower circumferential welds where the LS-DYNA triaxiality is greater than 0.33 (i.e., 1/DR > 1) during time steps when plastic deformation is occurring.

Plastic deformation during impact occurs in the time range of 0.018 to 0.022 seconds during the tip-over analysis. Figure 4-6 shows the effective plastic strain at the point of impact on the lid seal weld and Figure 4-7 shows the LS-DYNA triaxiality variable at the same time and location. The LS-DYNA triaxiality variable is highest at the 5:00 location (6:00 is impact) around the seal weld (1/DR = 6.3). However, the effective plastic strain in that location is only 0.48%, resulting in an adjusted strain of 0.48% x 6.3 = 3%. Directly in the impact zone, the LS-DYNA triaxiality is –2.9 (1/DR = 0.5) and the effective plastic strain is 36.8% in the elements representing the weld. The adjusted strain in the impact zone would be 36.8% x 0.5 = 18.4%. Therefore, when

stress triaxiality is considered during deformation, the adjusted strain in the impact zone is reduced but it is still more limiting than other locations around the seal weld. Note that the strain criteria proposed by Snow et al. (2009) does not give credit for compressive stress conditions that tend to increase the rupture strain of ductile materials. Therefore, the strain limit by that criterial would be only 0.67 x 40% = 26.8%.

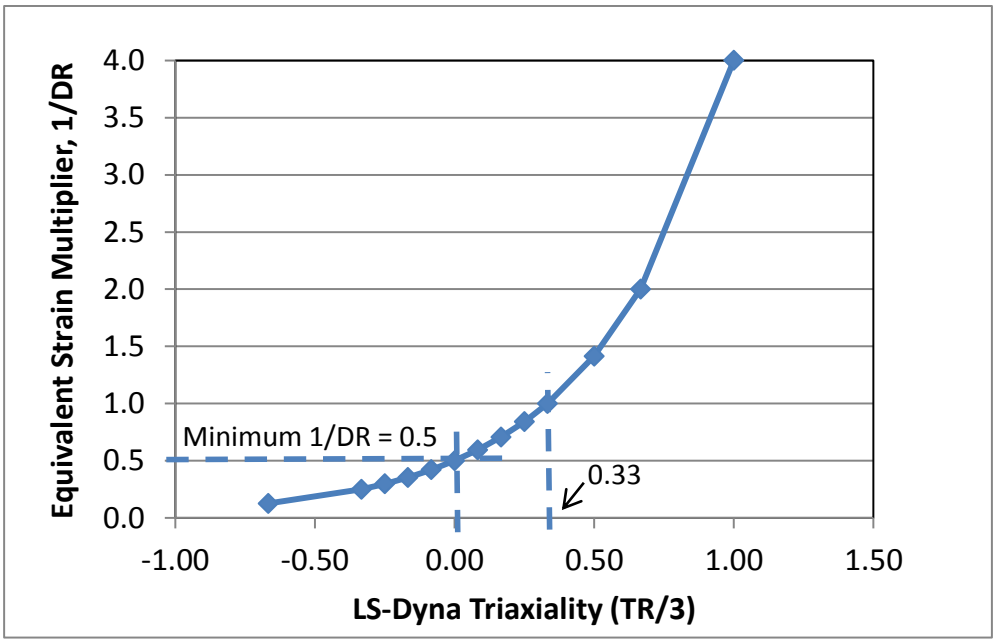

Figure 4-6: Effective strain multiplier, 1/DR, vs. LS-DYNA triaxiality variable.

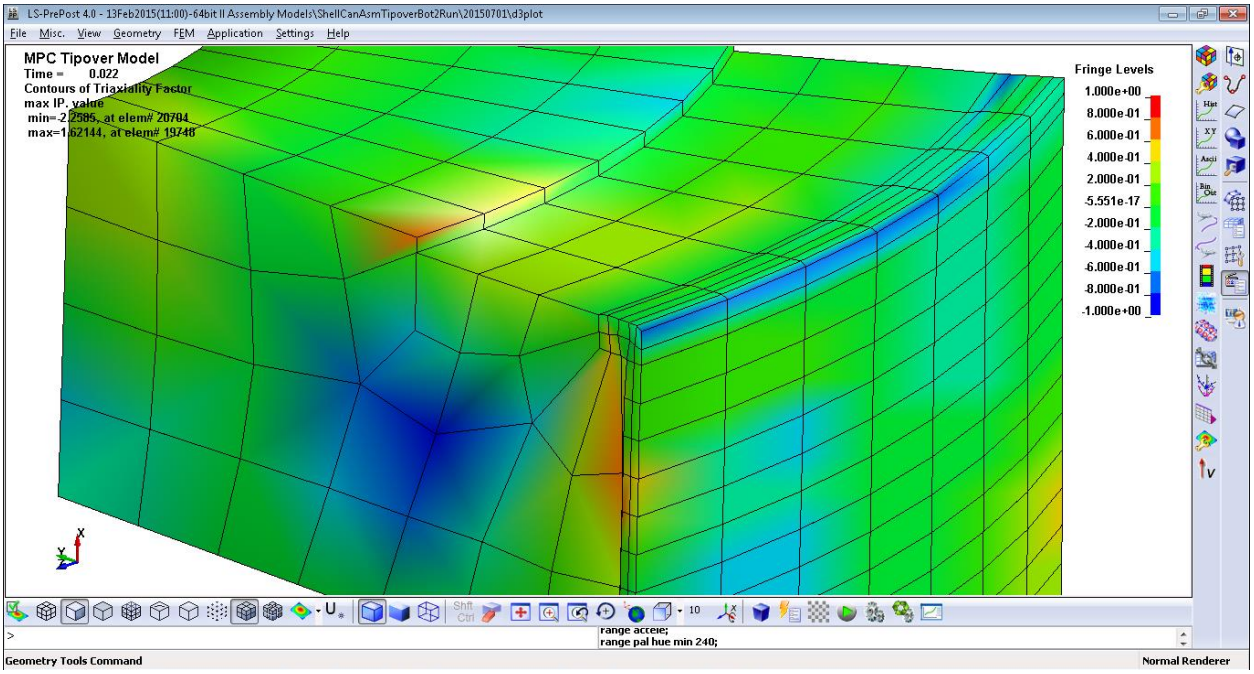

Figure 4-7: LS-DYNA triaxiality factor in the canister lid at impact (time = 0.022 seconds).

The LS-DYNA impact model was modified by removing elements that constitute half the weld line thickness to evaluate the effect of SCC at five worst-case locations determined from the undamaged model. Figure 4-8 shows the extent of material removed in the five locations. The relatively large volume of material that is removed at each location is a consequence of the coarse mesh density and is intended to be a first step in an analysis that will eventually consider a refined mesh and smaller flaw sizes. Location 1, at the 12:00 position of the lid seal weld, is on the side opposite the impact zone. Three elements were removed at location 1, which due to symmetry simulates a flaw that is 6 elements long with a total length to depth ratio, L/D=30. Only one element was removed at location 2 (the 6:00 positon in the lid seal weld), but due to symmetry the total flaw length is 2 elements, or L/D=10. Location 3 at the 12:00 position of the base plate weld has three elements removed at the symmetry plane for a total flaw length L/D=30. Location 4 at 2:30 on the base plate weld removes 3 elements for a total L/D=15. Finally, location 5 at the 6:00 position on the symmetry plane simulates a flaw with L/D=10. Figure 4-9 and Figure 4-10 show contour plots of the effective plastic strain and the LS-DYNA triaxiality variable during impact with the element removed at location 2 on the lid seal weld. Figure 4-11 and Figure 4-12 show the similar results with the element removed at location 5 on the base weld. Comparing the effective plastic strains in Figure 4-3 and Figure 4-9 shows that maximum plastic strain increases slightly and moves over one element when the element is removed from the weld line. Comparing Figure 4-7 and Figure 4-10 shows that the LS-DYNA triaxiality factor changes from approximately 0.2 to +0.6 in the element adjacent to the one removed at location 2.

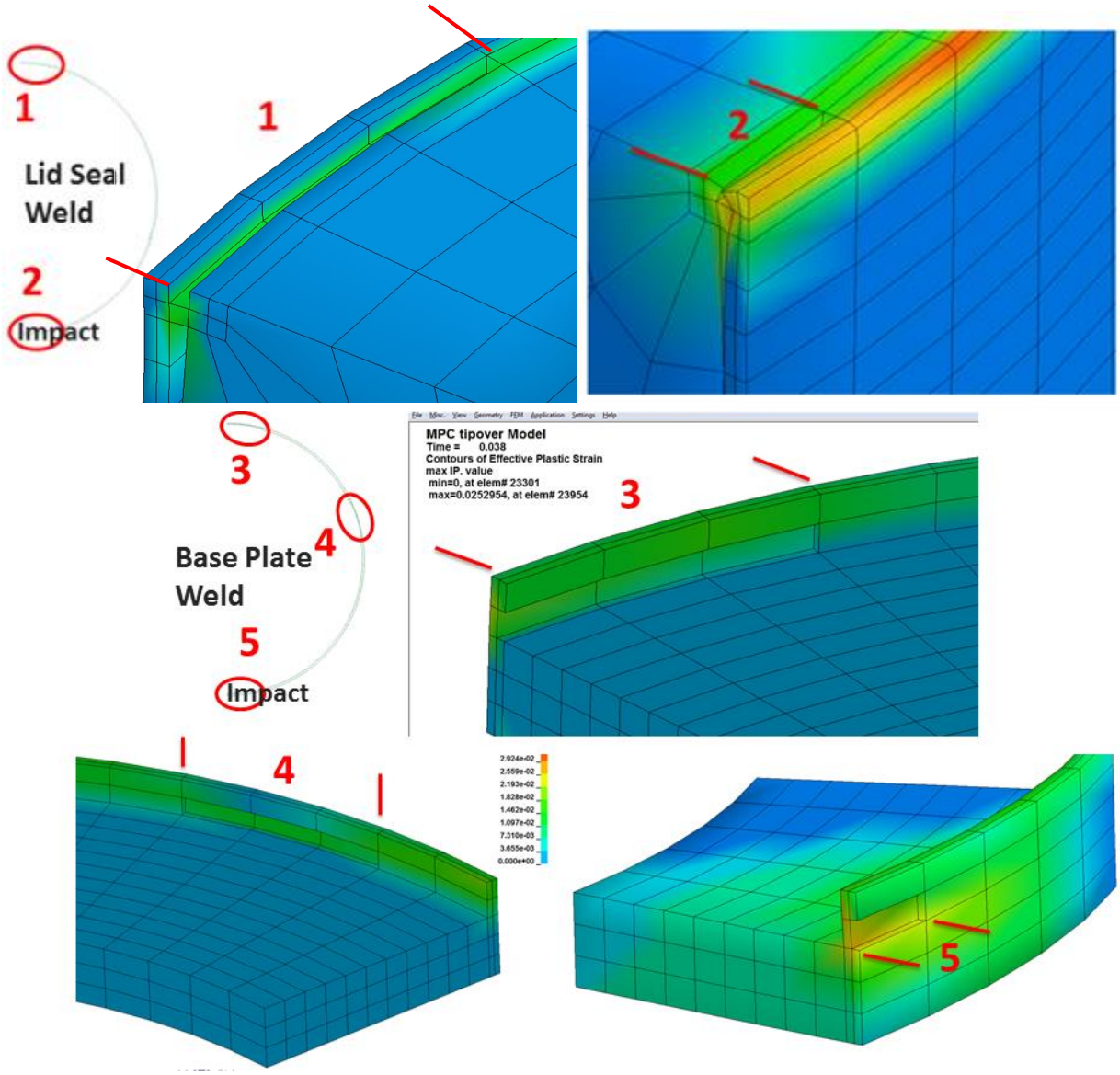

Figure 4-8: Locations of SCC damage simulated in the canister impact analysis.

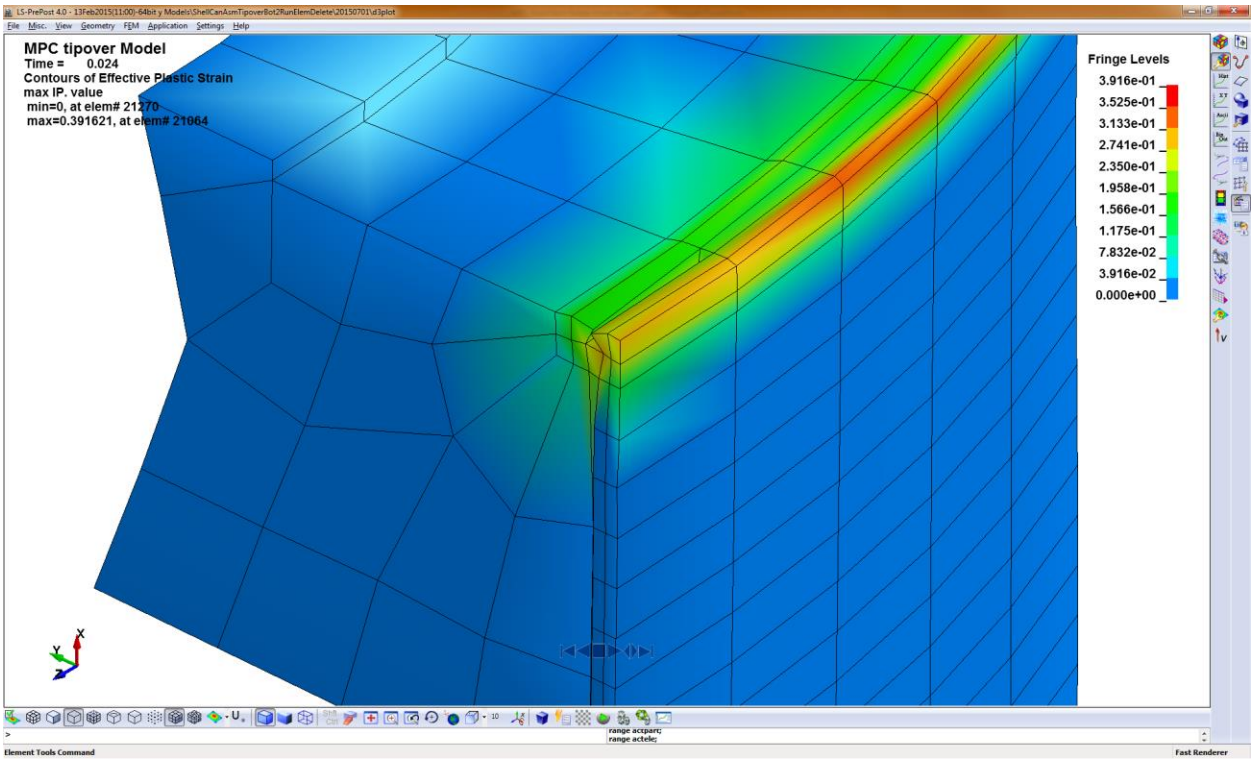

Figure 4-9: Location 2, effective plastic strain at impact after simulated SCC damage.

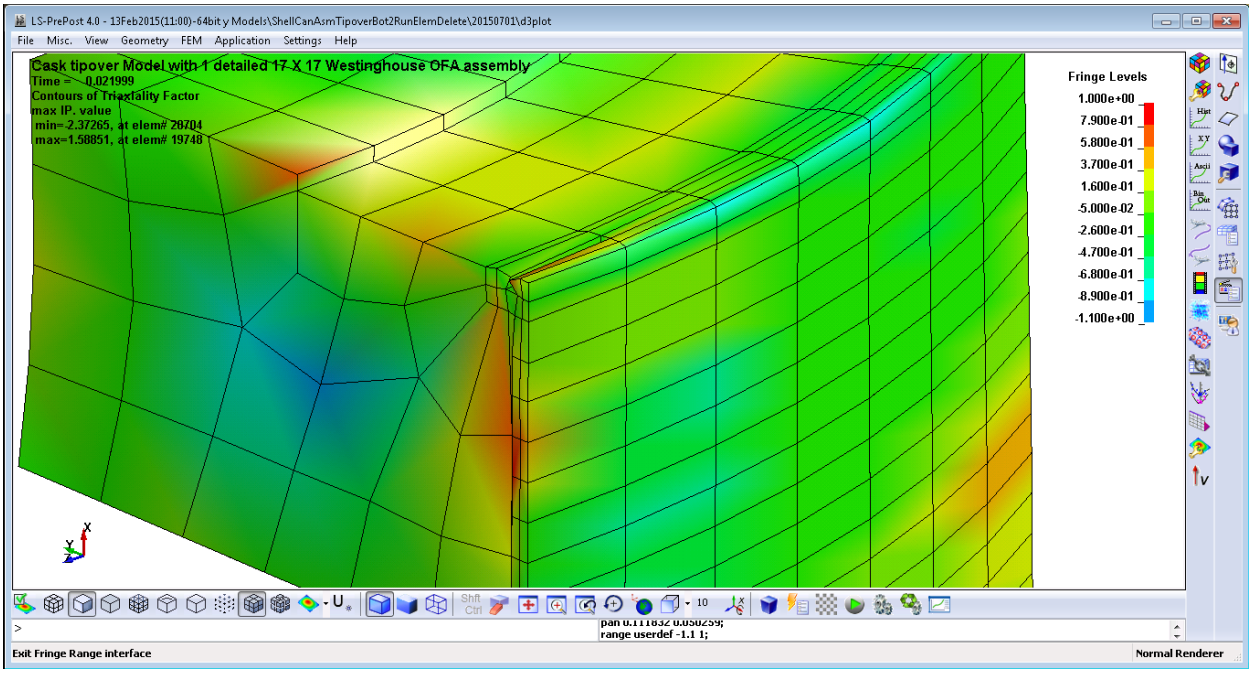

Figure 4-10: Location 2, triaxiality at impact after simulated SCC damage.

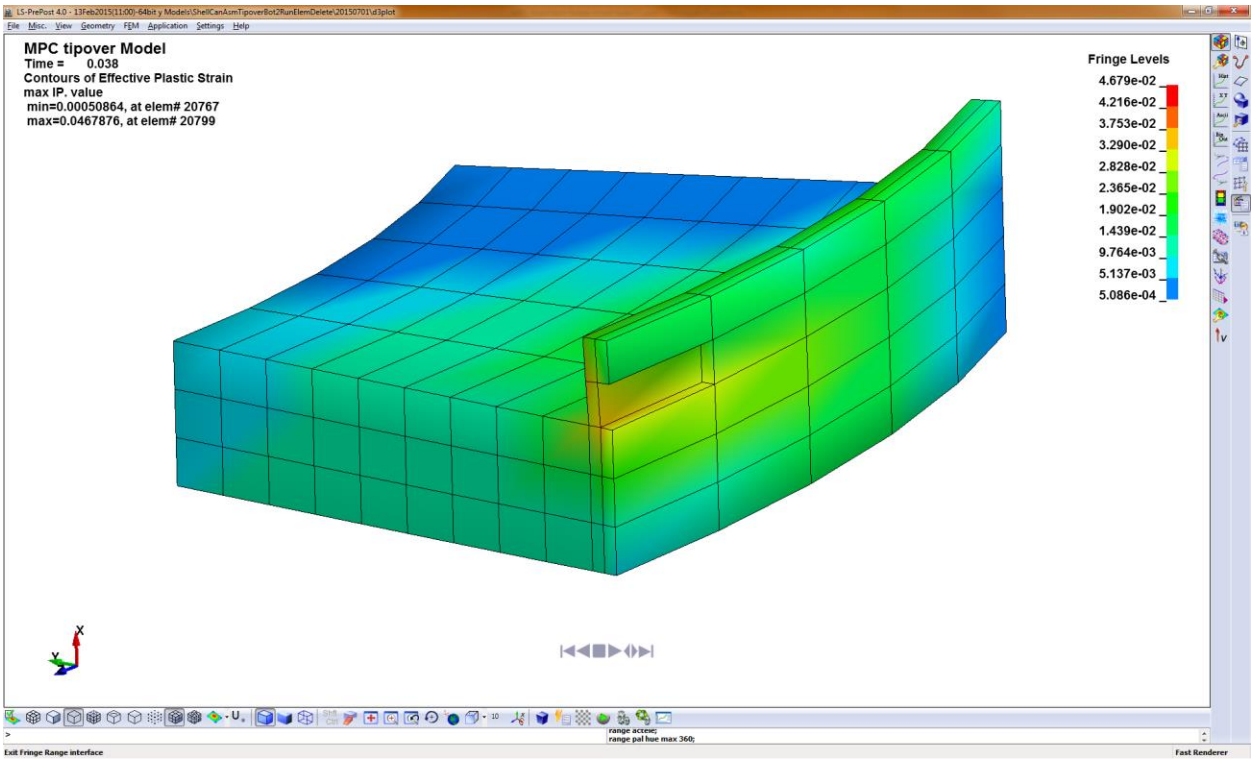

Figure 4-11: Location 5, effective plastic strain at impact after simulated SCC damage.

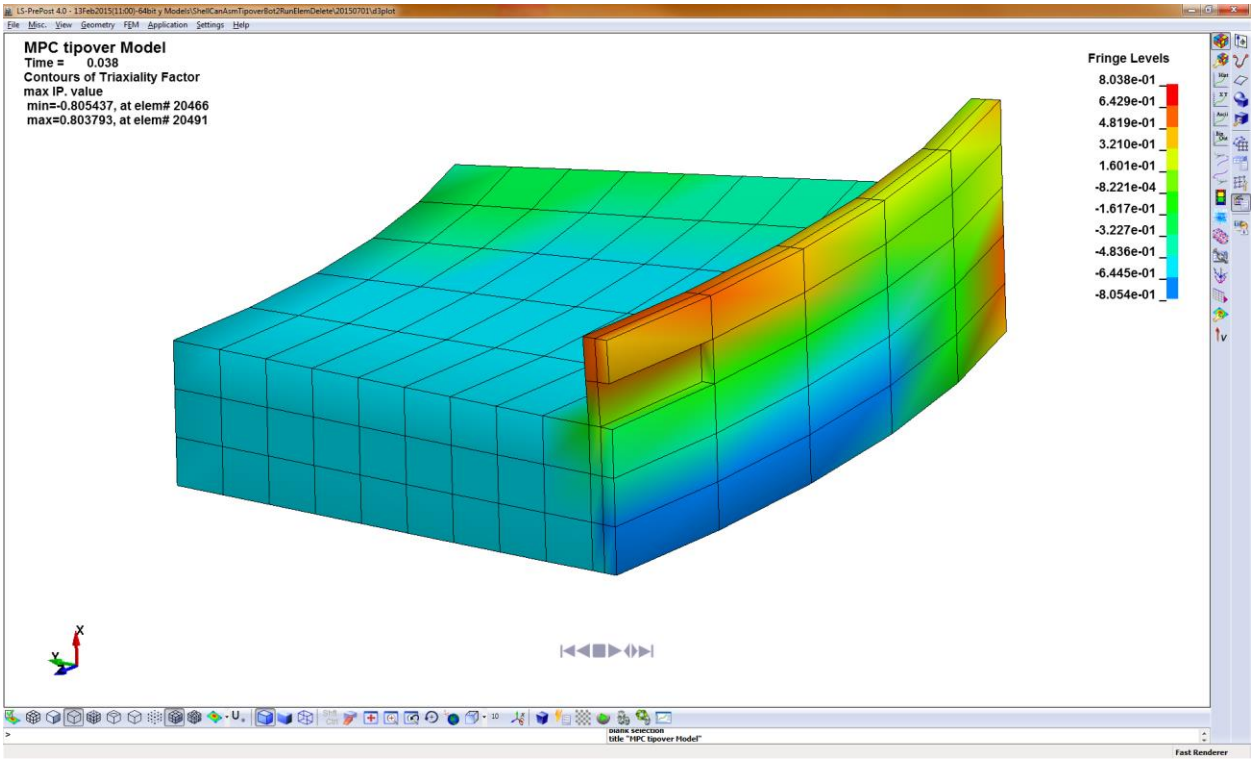

Figure 4-12: Location 5, triaxiality at impact after simulated SCC damage.

Figure 4-13 through Figure 4-16 show how removing material in the weld to simulating SCC damage changes the strains in the rings of elements around the lid and base plate welds. Figure 4-13 plots the effective plastic strains after impact for the outer ring of elements around the lid seal weld. The blue shaded bands indicate where flaws were simulated. The green triangles are the effective plastic strains of the model before elements have been removed. The red boxes show the similar strains in the model with elements removed from the outer ring at flaw locations 1 and 2. The element positions are numbered 1 to 36 from 6:00 to 12:00. The strain at element position 2 adjacent to flaw location 2 increases from about 11% to 13% with the assumed flaw. The blue diamonds in Figure 4-13 show the strains adjusted by the 1/DR factor. In the compressive impact zone (elements 1-7), the 1/DR adjustment reduces the effective strains by 50%. In other words, when comparing against the material tensile strain limit, the plastic strain achieved under hydrostatic compression acts as if it were only 50% of the calculated effective plastic strain. Outside of the impact zone, the plastic strains are 1% or less. Next to the simulated flaw at location 1, element 33 has a 1/DR factor greater than 1, so the adjusted strain is greater than the effective plastic strain. However, the adjusted strain is still only 1% at this remote location away from the impact zone. Figure 4-14 shows that strains are practically unchanged in the inner ring of elements even beneath the outer elements that were removed at flaw locations 1 and 2.

Figure 4-15 and Figure 4-16 plot the effective plastic strains and the 1/DR adjusted strains in the element rings around the base plate weld. Note that elements were removed from the inner ring at flaw locations 3 and 4 and from the outer ring at flaw location 5. Although the strains in Figure 4-15 are less than 5%, their increased magnitudes at elements 20-25 and 34-36 show how weld flaws at locations 4 and 5 would increase the strains that occur during impact. The 1/DR factors are also greater than 1 at these locations, so the deformation that occurs under triaxial tension is also more damaging than the same effective plastic strain under uniaxial tension. Figure 4-16 shows that the effective plastic strain at the element 1 impact zone decreases from 3.1% to 2.2% strain when the weld element is removed from the outer ring. However, the effect of that element removal changes the stress tensor significantly, which increases the 1/DR adjusted strain from 2.2% to 8.8%. Figure 4-16 also shows that the effective plastic strains decrease significantly in elements 2 through 7, beside flaw location 5, and again somewhat at elements 16 through 19. The triaxial tensile stress also increased the adjusted strain in elements 14 through 20 at the 3:00 to 4:00 o'clock position next to flaw location 4. This is due to increased local tensile stresses in the canister wall next to the restraint of the thick base plate.

Summarizing, Figure 4-13 through Figure 4-16 show that introducing damage in the lid seal weld and the base plate weld does not increase the previous maximum 39% strain in the impact zone of the lid seal weld. The analysis also shows that the significance of that 39% strain is lessened by the fact that it occurs under net compression where ductile materials tend to resist failure at higher strains than the uniaxial tensile failure strain that is typically reported. Although the strains are much lower in other areas of the lid and base plate welds, the analysis shows that introducing weld damage can change the canister impact resistance enough to alter not only the effective plastic strains but also the local stress distributions that can affect the local strain to failure.

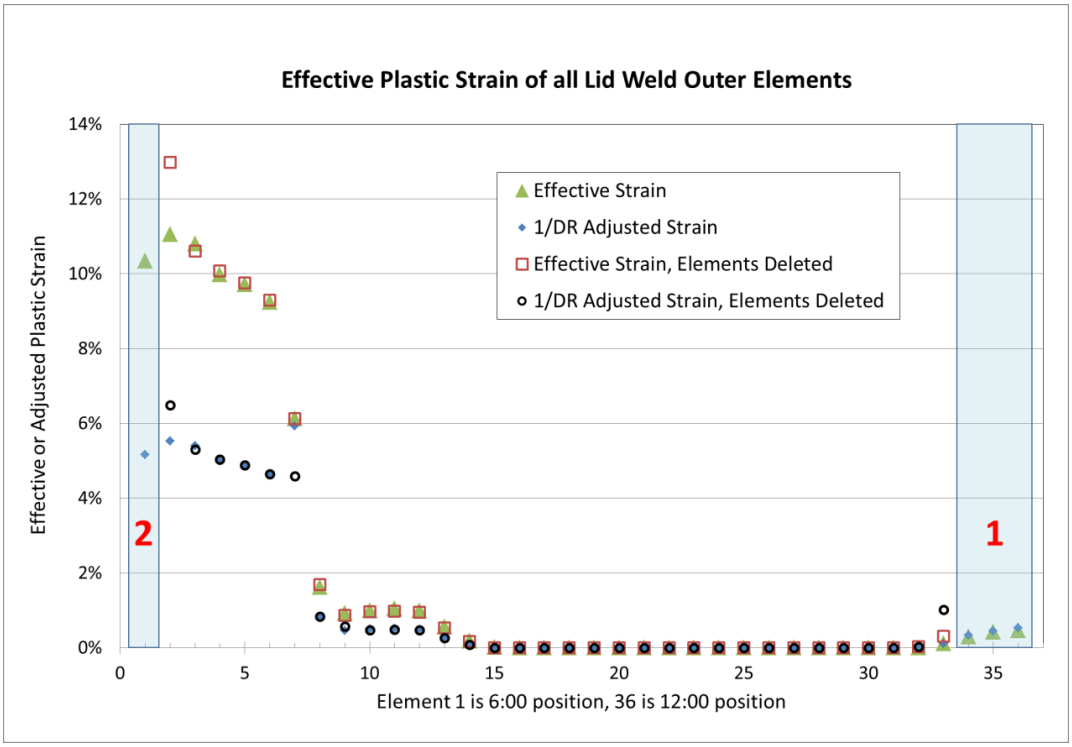

Figure 4-13: Effective plastic strains and 1/DR adjusted strains in the outer ring of lid weld elements. Comparison of results without SCC damage and with damage at time = 0.018 seconds.

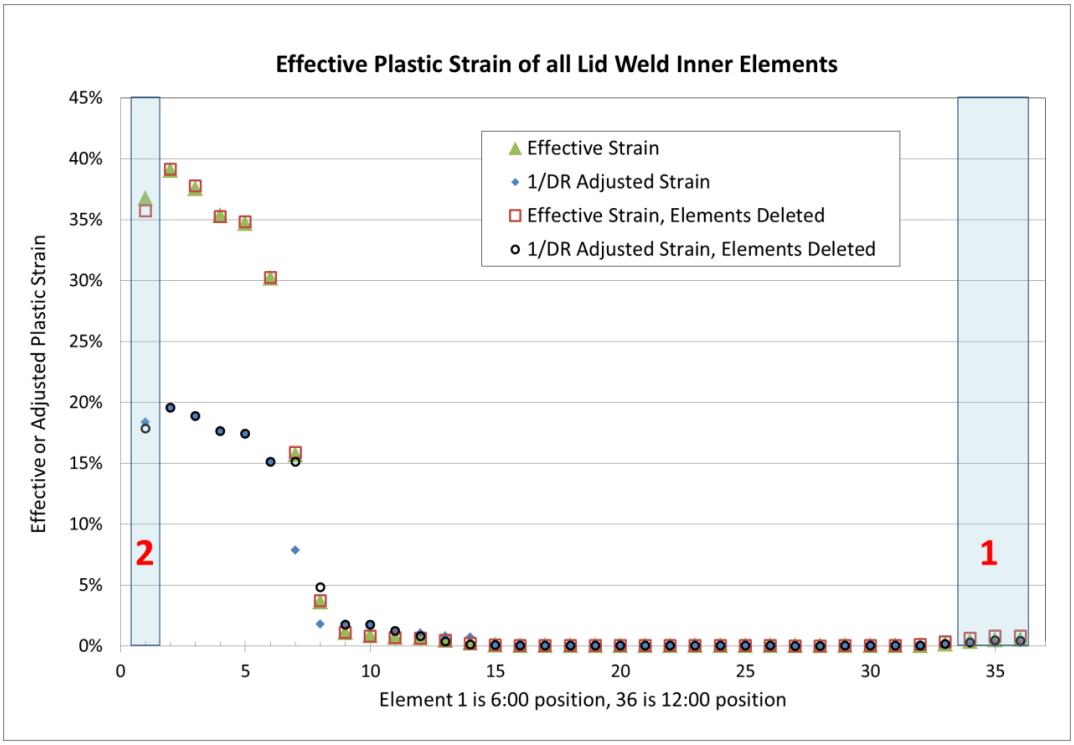

Figure 4-14: Effective plastic strains and 1/DR adjusted strains in the inner ring of lid weld elements. Comparison of results without SCC damage and with damage at time = 0.018 seconds.

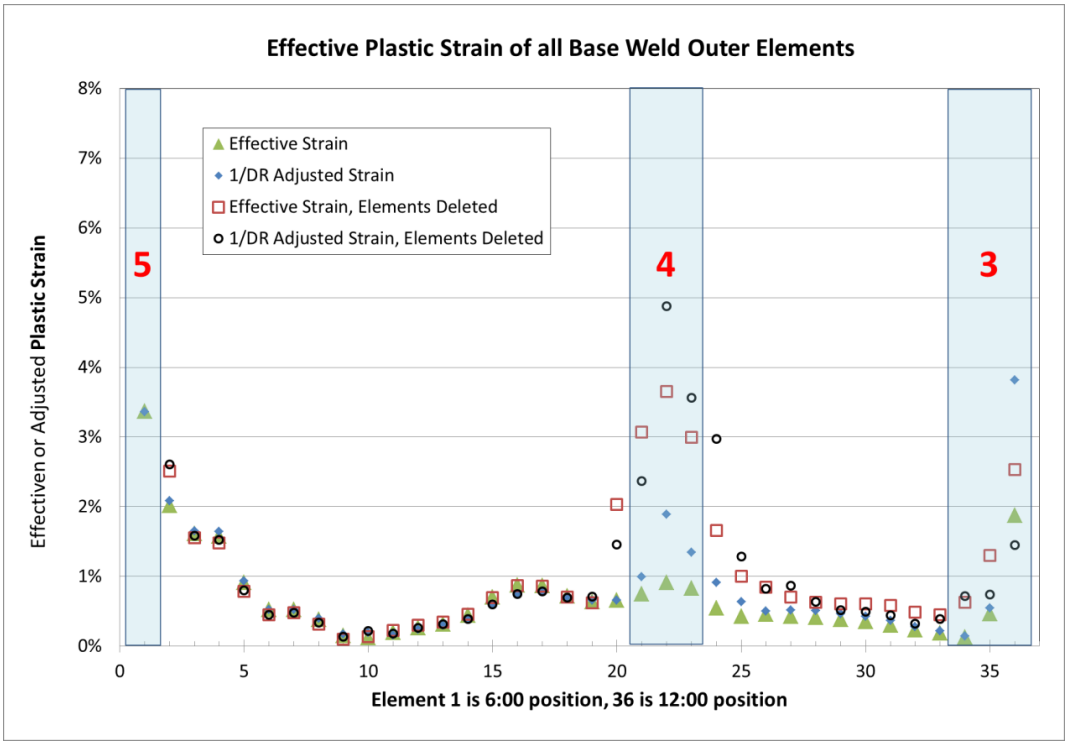

Figure 4-15: Effective plastic strains and 1/DR adjusted strains in the outer ring of base plate weld elements. Comparison of results without SCC damage and with damage at time = 0.036 seconds.

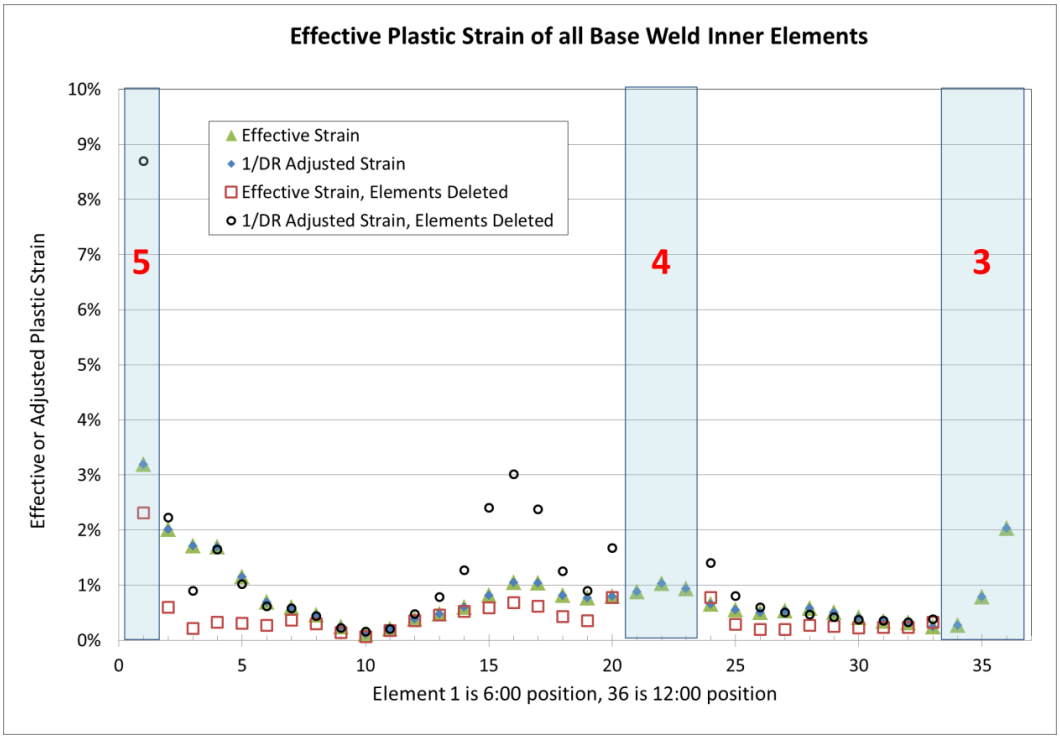

Figure 4-16: Effective plastic strains and 1/DR adjusted strains in the inner ring of base plate weld elements. Comparison of results without SCC damage and with damage at time = 0.036 seconds.

4.5 Comparison of Elastic-Plastic Fracture and Plastic Collapse Failure Modes

Alloy 304 and 316 stainless steels are highly ductile such that flaw growth typically occurs by elastic-plastic fracture or net section plastic limit load. This section compares the elastic-plastic fracture and plastic collapse failure modes to confirm that the plastic limit load will govern in the growth and failure of SCC-induced flaws in the wall of a multipurpose canister.

An elastic-plastic fracture analysis was performed to calculate the canister wall stress at which unstable crack growth would be predicted. The analytical solution of a circumferentially cracked cylinder was used to calculate the applied J-integral as a function of crack depth and applied axial stress. The applied J-integral curves for increasing stress levels were compared with the J-resistance curve for 304 stainless steel to estimate at what applied stress fracture would initiate and whether or not the crack would arrest or grow through-wall. EPRI report, NP-1931, *An Engineering Approach to Elastic-Plastic Fracture Analysis*, provides a detailed discussion of the J-estimation methods recommended for this analysis (Kumar et al. 1981). The total J-integral is estimated as the sum of the elastic and plastic components of *J*.

$$J = J_e + J_p \tag{3}$$

$$J_e = K_I^2 \frac{\left(1-\nu^2\right)}{E} \tag{4}$$

$$J_p = \alpha\sigma_0\varepsilon_0 c(a/b)H(a/L,n)\left(\frac{P}{P_0}\right)^{n+1} \tag{5}$$

where:

- K_I is the stress intensity factor from linear elastic fracture mechanics,
- ν is the Poisson's ratio,
- E is the elastic modulus,
- $\alpha, \sigma_0, \varepsilon_0, n$ are the parameters of the Ramberg-Osgood stress-strain curve,
- a = flaw depth, b = wall thickness, and c = remaining ligament (b-a),
- $H(a/L,n)$ is the plastic J influence function as a function of crack depth and the Ramberg-Osgood exponent, n, and
- $\left(\frac{P}{P_0}\right)^{n+1}$ is the ratio of the applied load to the perfectly-plastic limit load, P_0.

NP-1931 (Kumar et al. 1981) provides the Ramberg-Osgood stress strain parameters for 304 stainless (Figure 4-17) as well as the plastic J influence functions, $H(a/L,n)$, for circumferentially cracked cylinders. A detailed example is also presented in NP-1931 where this J estimation method is applied to the circumferential cracking of a large 304 stainless cylinder under axial loading. That example was reproduced in an Excel spreadsheet and the matching results are plotted in Figure 4-18. Note that the large crack depths considered in the Figure 4-18 example correspond to a large cylinder similar in size to a reactor pressure vessel (90-inch inner radius with a 9-inch wall thickness).

The literature was also reviewed to compile J-resistance curves for 304 stainless steel tested under static and dynamic load conditions (Figure 4-19). Sampath et al. (1981) tested sharp-notched, 3-point bend specimens of two different thicknesses at static (9×10^{-6} m/sec) and dynamic (1.8 m/sec) displacement rates. Figure 4-20 shows that impact-loaded specimens exhibited a higher fracture resistance than did the samples where static loads were applied. Kanninen et al. (1982) present similar results in EPRI NP-2347 and conclude that the use of static J-resistance curves in dynamic impact analysis is conservative. Therefore, the lower bound J-resistance curve in Figure 4-20 (Sampath, Static, 3-pt, t=8.5 mm) was conservatively used in the elastic-plastic fracture analysis presented here.

The J-integral evaluation for the multipurpose canister was conducted by substituting the canister body dimensions into the spreadsheet used for the demonstration calculations in Figure 4-18. Figure 4-21 shows the calculated J-integral vs. J-resistance curves for the canister inner radius (86.4 cm) and wall thickness (12.7 mm) dimensions. Figure 4-21 shows the J-resistance curve

beginning at an initial crack depth of 6.35 mm (50% of the 12.7 mm wall thickness). The J-integral curves that intersect and cross below the J-resistance curve correspond to tensile stress values in the cylinder body that would result in stable crack growth from the initial crack depth to the increased depth where the J-integral and J-resistance curves first intersect. Using this criterion, the tensile stress curves in Figure 4-21 below 250 MPa would result in a small amount of stable crack growth. The blue curve at 275 MPa does not intersect the J-resistance curve, and therefore an applied stress of 275 MPa would result in unstable crack growth.

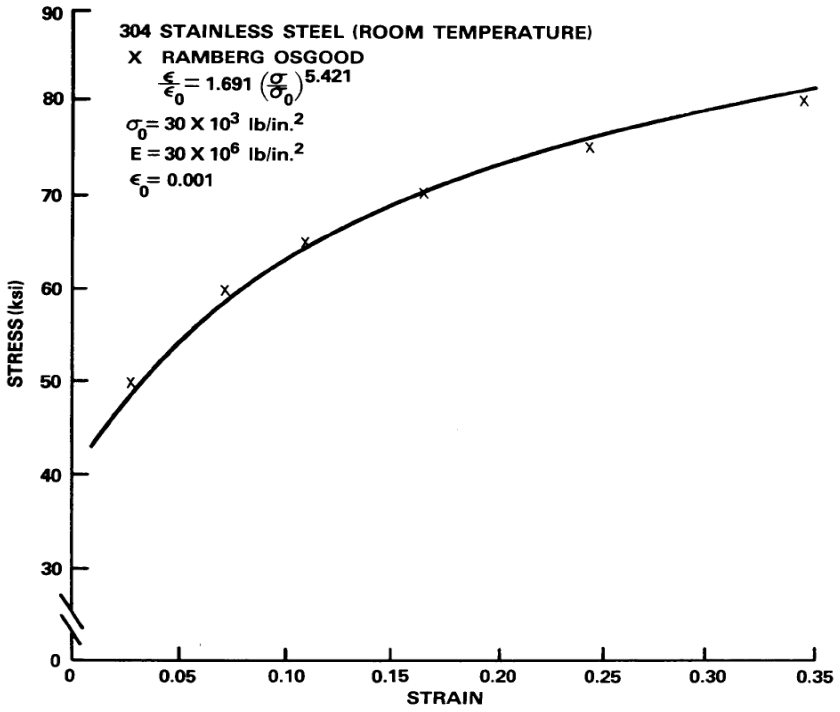

Figure 4-17: A Ramberg-Osgood stress-strain curve for 304SS from Kumar et al. (1981).

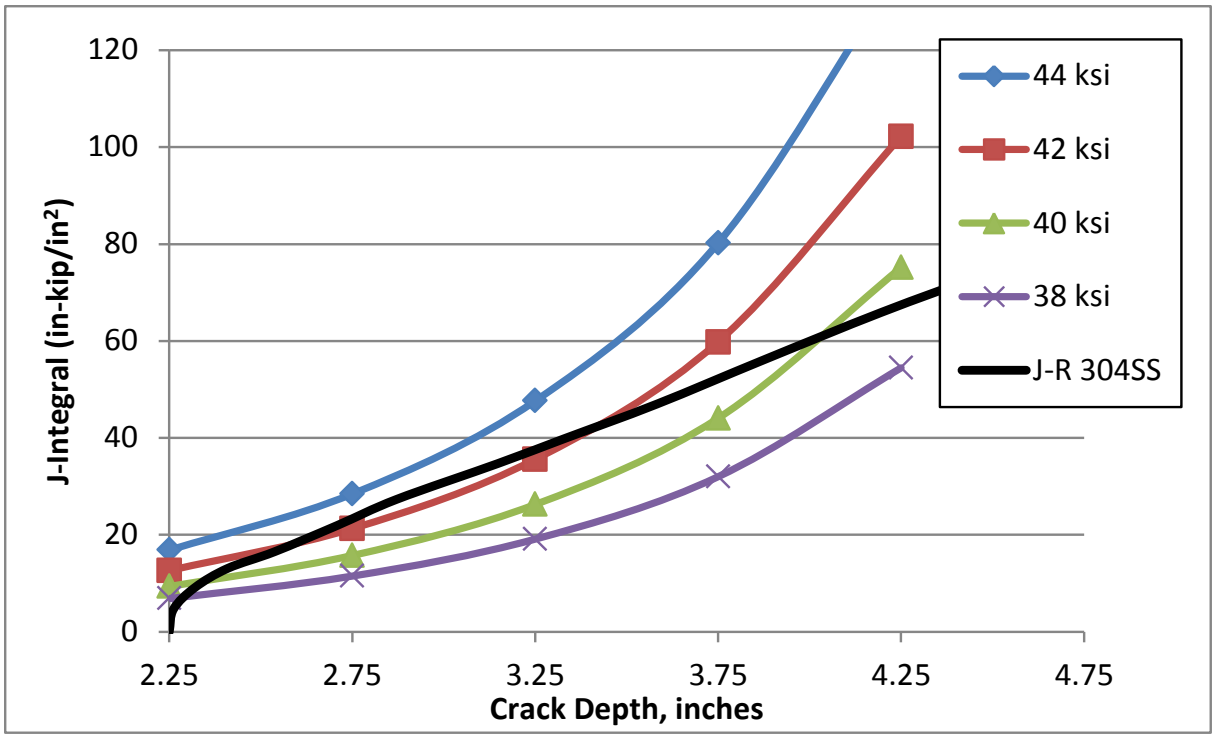

Figure 4-18: Confirmation of J-integral estimation results for a large cylinder with a circumferential crack from Kumar et al. (1981).

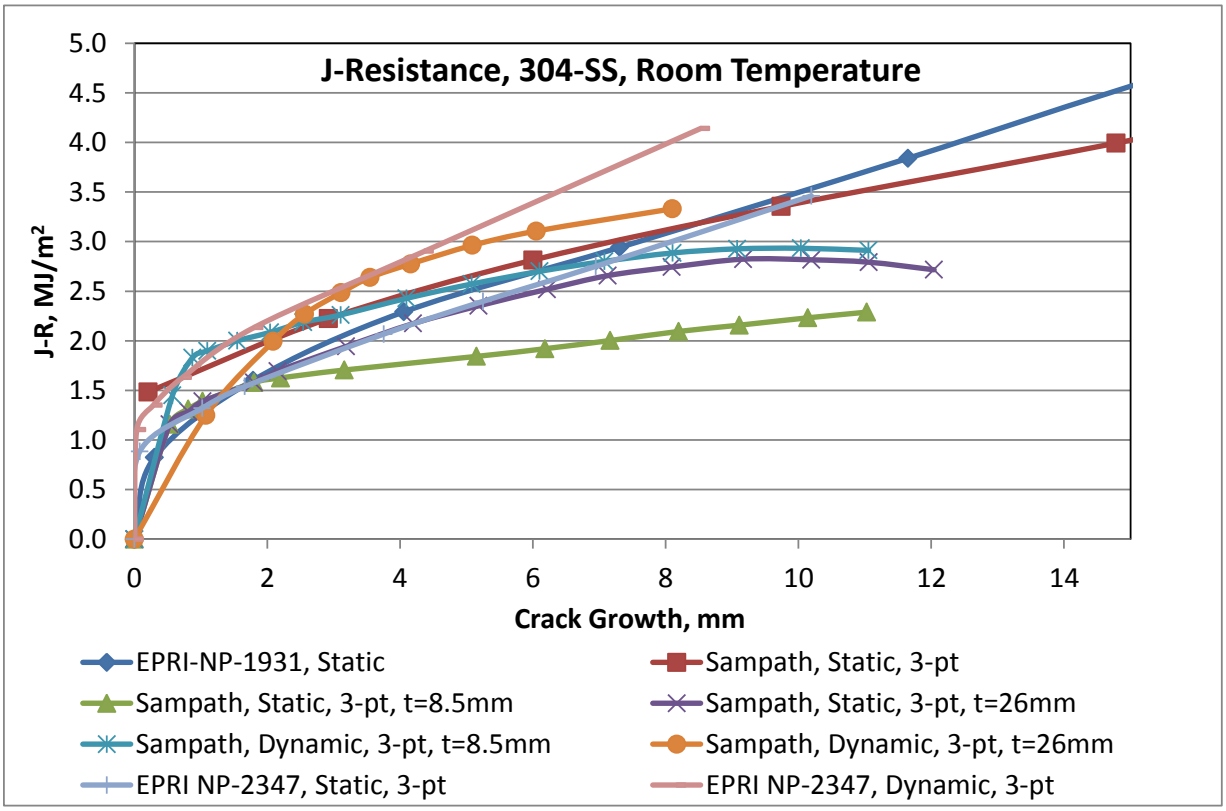

Figure 4-19: Comparison of J-resistance curves from several sources.

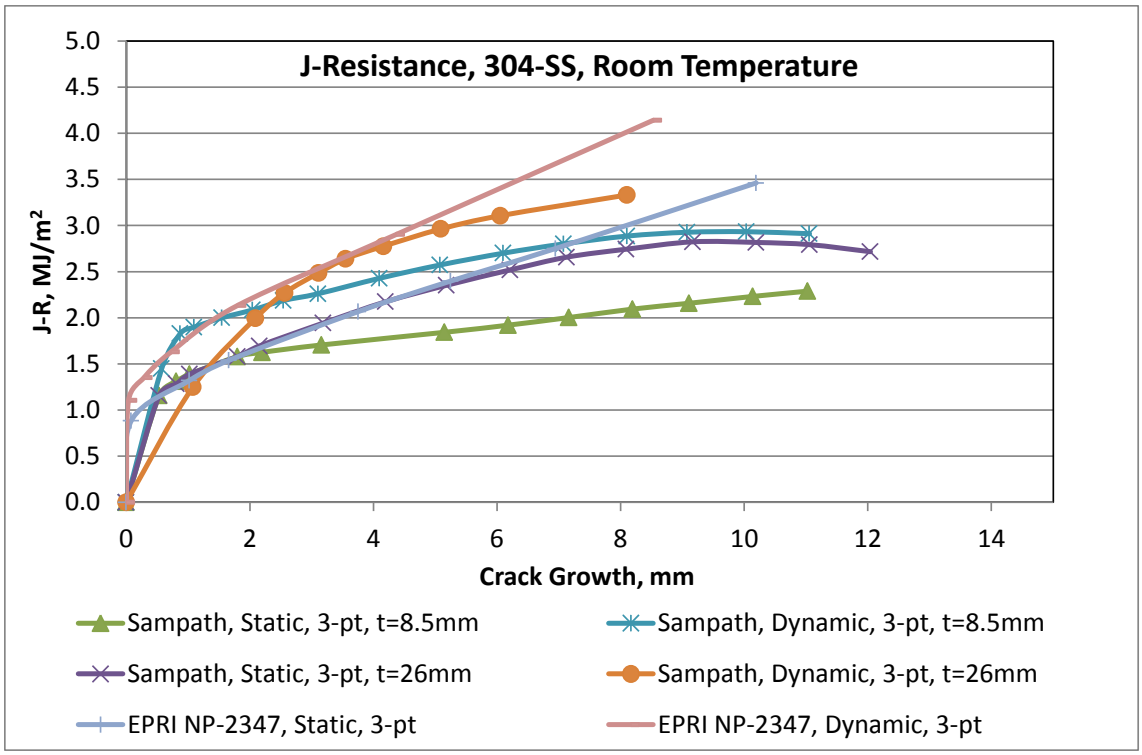

Figure 4-20: A Comparison of J-resistance curves for 304 stainless steel from static and dynamic tests.

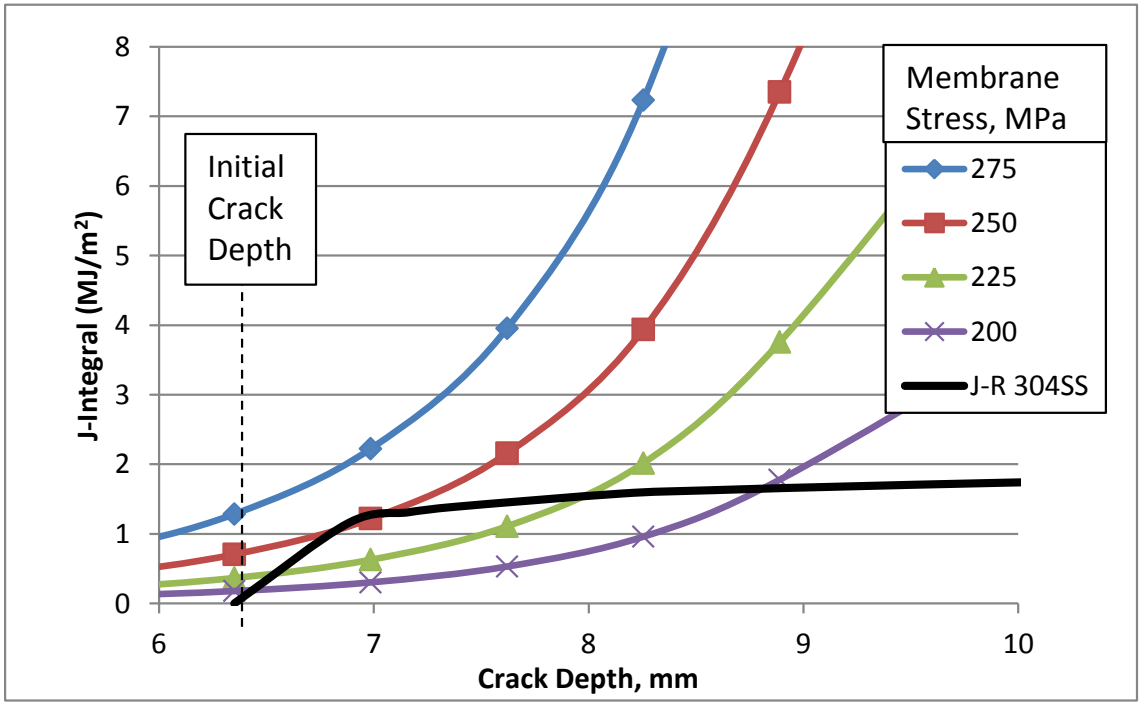

Figure 4-21: J-integral vs. J-resistance curves for the multipurpose canister inner radius (86.4 cm) and wall thickness (12.7 mm).

4.6 Plastic Limit Load Analysis

The plastic limit load failure criteria in Section XI, Appendix C of the ASME Boiler & Pressure Vessel Code (ASME 2013a) can be used to estimate the flaw depth at plastic collapse that corresponds to the material flow stress in the cylindrical canister body. For a full circumferential crack, the membrane stress, $\sigma_{m,}$ at incipient plastic collapse is expressed as:

$$\sigma_m = \frac{\sigma_f}{SF_m}\left(1 - \frac{a}{t}\right) \tag{6}$$

where,

SF_m = Structural safety factor for service levels A-D, SF_m(D) = 1.3
SF_m = 1.0 at incipient collapse
σ_f = flow stress $= \frac{\sigma_y + \sigma_u}{2}$
σ_y = yield stress
σ_u = ultimate stress
a = through thickness crack depth
t = vessel wall thickness

Rearranging equation (6), the maximum allowable crack depth of a full circumferential crack at incipient limit load failure is equal to

$$\frac{a}{t} = \left(\frac{\sigma_f - SF_m\sigma_m}{\sigma_f}\right) \tag{7}$$

The minimum yield and ultimate strengths of 304 stainless at room temperature are listed as 172 MPa (25 ksi) and 448 MPa (65 ksi) in Section II of the ASME code (ASME 2013b). This gives a flow stress of 310 MPa (45 ksi). Equation (7) provides a conservative estimate of the maximum flaw depth for plastic collapse at the tensile stress for unstable crack growth that was calculated in the elastic-plastic fracture analysis. For a given applied stress, plastic collapse would be expected to occur before the onset of unstable crack growth if the flaw depth for plastic collapse is less than the flaw depth for unstable elastic-plastic fracture.

Equation (6) also gives the tensile membrane stress at plastic collapse as a function of the flow stress and the ratio of flaw depth to thickness. Figure 4-22 shows that for a flow stress of 310 MPa and initial a/t=0.5 the membrane stress at incipient plastic failure is only 155 MPa. Comparing this to the elastic-plastic fracture analysis in Figure 4-21 (stable crack growth and arrest for applied stresses below 250 MPa) shows that the plastic collapse failure mode is more limiting than elastic-plastic fracture. Therefore, the ductile stainless steel of the canister body has high toughness such that the flawed sections will deform plastically without crack extension. Plastic deformations will be limited by the tensile elongation divided by the ductility factor as described previously in this report.

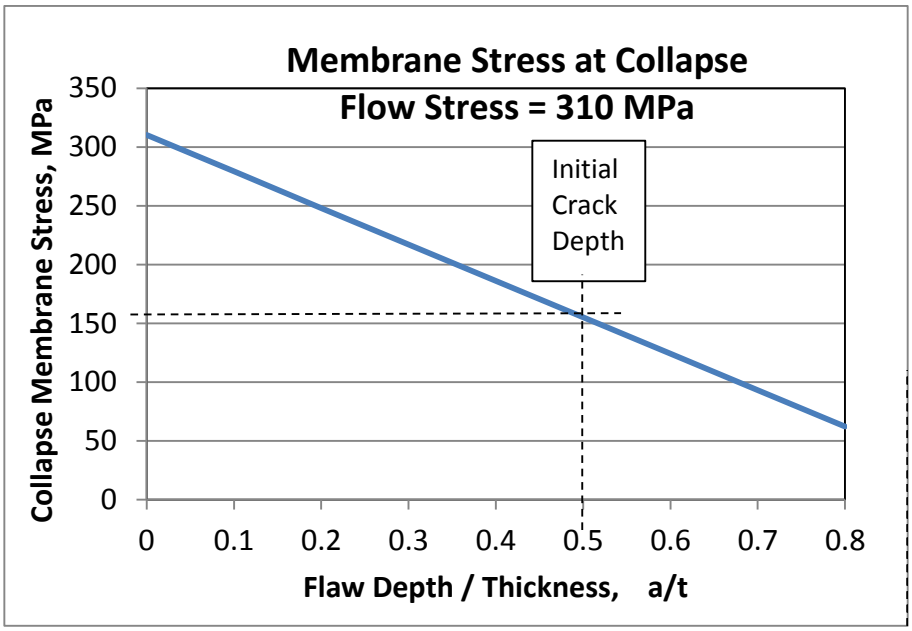

Figure 4-22: Membrane stress at plastic collapse vs. flaw depth ratio, a/t.

4.7 Summary and Conclusions

A canister tip-over accident was modeled to estimate the significance of stress corrosion cracking on the integrity of welds in a multi-purpose canister for long-term storage of used nuclear fuel assemblies. The analysis assumed that SCC had occurred to a crack depth of one-half the canister wall thickness. A detailed finite element model of the canister geometry and the distributed mass of the contained fuel was used to estimate the plastic strains from the tip-over accident. The model was first run without weld flaws to identify where SCC damage might be the most significant. Two locations in the lid seal weld and three locations in the circumferential base plate weld were identified for further damage analysis. The magnitude of effective plastic strain was used as the primary damage level criteria. The triaxial stress state during plastic deformation was also evaluated to calculate adjusted plastic strains for comparison with the estimated tensile elongation strain of 40%.

SCC flaws were simulated by removing elements along the weld line that represented 50% of the wall thickness. The results show that introducing damage in the lid seal weld and the base plate weld did not increase the previous maximum 39% strain in the impact zone of the lid seal weld. Also, the maximum plastic strain occurs in the impact zone where net compression tends to increase the local rupture strain compared to the uniaxial tensile failure strain that is typically reported for ductile materials. Although the strains are much lower in other areas of the lid and base plate welds, the analysis shows that introducing weld damage can change the effective plastic strains and the local stress distributions enough to affect the local strain to failure.

We also presented elastic-plastic fracture and plastic collapse analyses that show that even in the presence of cracking, plastic deformation of the ductile 304 stainless steel canister body is the expected failure mode rather than elastic-plastic fracture.

4.8 Future Work

The accuracy of the finite element model is limited by the mesh refinement of the model, especially in the weld line where SCC damage was postulated. Further work is recommended to refine the mesh in this area to confirm the accuracy of the current results and conclusions.

The current model removes finite elements as a first approximation of SCC damage. This is a good first approximation of the crack opening effect, but it is less accurate in compression. A closer approximation creating double-nodes along the weld line and applying contact conditions between the crack faces of the adjacent element pairs is needed. This approach would better approximate the closing of a tight crack in compression, and it would maintain the crack opening mode under tensile loads.

The maximum strains in the tip-over accident are compressive in the impact zone. The tensile strains, which are more damaging to the canister, were calculated to be less than 5% in the base plate weld. Other canister accidents such as an end-drop into the canister over-pack could also be analyzed to determine if higher levels of damage are predicted.

5.0 CONCLUSIONS

This progress report discusses the modeling work that was accomplished this fiscal year in three separate areas that are valuable to the UFDC program. Modeling fuel cladding using beam elements in a highly detailed fuel assembly model is an important topic in both storage and transportation. Stress corrosion cracking is an important materials topic, and modeling helps to estimate its significance.

The cladding modeling options study demonstrates that the LS-DYNA beam element formulation has some effect on model results. The Belytschko-Schwer integrated beam element formulation with 4x4 Gauss quadrature was identified as the most accurate formulation to match a closed-form beam bending solution using a section of cladding as a basis. However, the default beam formulation was not largely different, achieving error bands of ±5% while the most accurate formulation was within ±1%. These results indicate that even the default beams offer a reasonable level of accuracy.

When the high-accuracy beam element formulation was applied to the tip-over load case, it had a surprisingly large effect on the calculated cladding response. The default beam element model from FY14 predicted zero cladding failures, but the upgraded FY15 model predicted widespread cladding failure. The three sets of tip-over results are reported here for the purpose of reporting progress only, as the unexpected results are still being reviewed for potential errors. When this study continues in FY16, the first priority will be to determine the validity of the calculated results and revise them if necessary.

Finally, stress corrosion cracking in the MPC welds was evaluated. This study used a combination of classical crack propagation and section collapse analyses in conjunction with LS-DYNA explicit dynamic analyses to evaluate the potential impact of stress corrosion cracking on the MPC containment boundary. For the tip-over load case that was analyzed, elastic-plastic fracture and plastic collapse analyses show that even in the presence of cracking, plastic deformation of the ductile 304 stainless steel canister body is the expected failure mode rather than elastic-plastic fracture.

6.0 REFERENCES

Adkins, HE, Jr, KJ Geelhood, BJ Koeppel, NA Klymyshyn, and SE Sanborn. 2012. *Used Nuclear Fuel Loading and Structural Performance Under Normal Conditions of Transport – Demonstration of Approach and Results on Used Fuel Performance Characterization*. PNNL-22825, Pacific Northwest National Laboratory, Richland, Washington.

ASME. 2013a. ASME Boiler & Pressure Vessel Code, Section XI, *Inservice Inspection*, Appendix C. American Society of Mechanical Engineers. New York, New York.

ASME. 2013b. ASME Boiler & Pressure Vessel Code, Section II, Part D, *Properties, Materials*. American Society of Mechanical Engineers. New York, New York.

Caseres, L and TS Mintz. 2010. *Atmospheric Stress Corrosion Cracking Susceptibility of Welded and Unwelded 304, 304L, and 316L Austenitic Stainless Steels Commonly Used for Dry Cask Storage Containers Exposed to Marine Environments.* NUREG/CR-7030. Southwest Research Institute. San Antonio, Texas.

Enos, DG, CR Bryan, and KM Norman. 2013. *Data Report on Corrosion Testing of Stainless Steel SNF Storage Canisters, Fuel Cycle Research and Development*. FCRD-UFD-2013-000324, SAND2013-8314. Sandia National Laboratory, Albuquerque, New Mexico.

He, X, TX Mintz, R Pabalan, L Miller, and G Oberson. 2013. *Assessment of Stress Corrosion Cracking Susceptibility for Austenitic Stainless Steels Exposed to Atmospheric Chloride and Non-Chloride Salts*. NUREG/CR-7170. Southwest Research Institute. San Antonio, Texas.

Kanninen, MF, A Zahoor, G Wilkowski, I Abou-Sayed, C Marschall, D Broek, S Sampath, H Rhee, and J Ahmed. 1982. *Instability Predictions for Circumferentially Cracked Type-304 Stainless Steel Pipes Under Dynamic Loading.* EPRI NP-2347, Volume 1, Research Project T118-2. Prepared by Battelle, Columbus Laboratories for Electric Power Research Institute, Palo Alto, California.

Klymyshyn, NA, NK Karri, HE Adkins, and BD Hanson. 2013. *Structural Sensitivity of Dry Storage Canisters.* FCRD-UFD-2013-000378, PNNL-22814, Pacific Northwest National Laboratory, Richland, Washington.

Klymyshyn, NA, NK Karri, HE Adkins, Jr, and BD Hanson. 2014a. *Structural Uncertainty of Used Nuclear Fuel in Dry Storage Canisters*. PNNL-23710, Pacific Northwest National Laboratory, Richland, Washington.

Klymyshyn NA, PJ Jensen, SE Sanborn, and BD Hanson. 2014b. *Fuel Assembly Shaker and Truck Test Simulation*. PNNL-23688, Pacific Northwest National Laboratory, Richland, Washington.

Kumar, V, MD German, and CF Shih. 1981. *An Engineering Approach for Elastic-Plastic Fracture Analysis.* EPRI NP-1931. Project 1237-1, Topical Report July 1981. Prepared for EPRI by General Electric Company, Schenectady, New York.

LSTC. 2013. *LS-DYNA® Keyword User's Manual, Volume II, Material Models*, Version R7.0, Livermore Software Technology Corporation, Livermore, California.

Malliakos, A. 2007. *A Pilot Probabilistic Risk Assessment of a Dry Cask Storage System at a Nuclear Power Plant.* NUREG-1864. U.S. Nuclear Regulatory Commission. Washington, D.C.

Manjoine, MJ. 1982. *Creep Rupture Behavior of Weldments.* Welding Journal: Research Supplement, Vol. 61, No. 2, American Welding Society, Miami, Florida, February 1982.

NRC, EPRI. 2011. *Models and Inputs Developed for Use in the xLPR Pilot Study*. U.S. NRC Office of Nuclear Regulatory Research, Washington, D.C. Electric Power Research Institute, Palo Alto, California.

Sampath, SG, IS Abou-Sayed, D Broek, C Marshall, A Zahoor, and MF Kanninen. 1981. "The Analysis of Stable Crack Growth in Type 304 Stainless Steel." Battelle Columbus Laboratories, Columbus, Ohio. In *Proceedings of Advances in Fracture Research, International Conference on Fracture*, Cannes, France, pp. 1759-1767.

Shimskey RW, BD Hanson, CA Lavender, SG Pitman, EV Stephens, PJ MacFarlan, and ME Dahl. 2014. *FY 2014 PNNL Zr Cladding Testing Status Report*. (FCRD-UFD-2014-000054, PNNL-23594), Pacific Northwest National Laboratory, Richland, Washington.

Snow, SD, DK Morton, EL Pleins, and R Keeting. 2009. "Strain-Based Acceptance Criteria for Energy-Limited Events." In *Proceedings of the 2009 ASME Pressure Vessels and Piping Division Conference*, July 26-30, 2009, Prague, Czech Republic.